The origin of the potassium-rich annular zones at the Bosumtwi impact structure, Ghana, investigated by field study, radiometric analysis, and first cosmogenic nuclide data

Cheikh Ahmadou Bamba Niang, David Baratoux, Pierre Rochette, Regis Braucher, Wolf Uwe Reimold, Philippe Lambert, Dinna Pathe Diallo, Vincent Regard, Sebastien Carretier, Mark W. Jessell, et al.

The Meteoritical Society

Meteoritics & Planetary Science 57, Nr 3, 702–729 (2022)
doi: 10.1111/maps.13788

The origin of the potassium-rich annular zones at the Bosumtwi impact structure, Ghana, investigated by field study, radiometric analysis, and first cosmogenic nuclide data

Cheikh Ahmadou Bamba NIANG[1,2,3*], David BARATOUX[4,10], Pierre ROCHETTE[3], Regis BRAUCHER[3], Wolf Uwe REIMOLD[5], Philippe LAMBERT[6], Dinna Pathe DIALLO[1], Vincent REGARD[4], Sebastien CARRETIER[4], Mark W. JESSELL[7], Gayane FAYE[8], and Christian KOEBERL[9]

[1]Département de Géologie, Université Cheikh Anta Diop, Dakar, Dakar, Senegal
[2]Institut Fondamental d'Afrique Noire Cheikh Anta Diop, Dakar, Senegal
[3]Aix-Marseille Univ, CNRS, IRD, INRAE, CEREGE, Aix-en-Provence, France
[4]Géosciences Environnement Toulouse, CNRS, IRD & Université de Toulouse, France
[5]Institute of Geosciences, Laboratory of Geochronology and Isotope Geology, University of Brasília, Brasília, Brazil
[6]CIRIR—Center for International Research and Restitution on Impacts and on Rochechouart, 87600 Rochechouart, France
[7]Centre for Exploration Targeting, School of Earth Sciences, The University of Western Australia, 35 Stirling Highway, Crawley, Western Australia 6009, Australia
[8]Institut des Sciences de la Terre, Laboratoire de Télédétection Appliquée, Université Cheikh Anta Diop, Dakar, Senegal
[9]Department of Lithospheric Research, University of Vienna, Althanstrasse 14, A-1090 Vienna, Austria
[10]UFR Sciences de la Terre et des Ressources Minières, Université Félix Houphouët-Boigny, Abidjan, Côte d'Ivoire
*Corresponding author. E-mail: cabniangeos@gmail.com

(Received 22 February 2021; revision accepted 03 January 2022)

Abstract–The 10.5-km-diameter, 1 Ma Bosumtwi impact structure in Ghana is one of the youngest, large impact structures known on Earth. The preservation of the morphology of its ejecta deposits, with an annular moat and outer ridge resembling those of rampart impact craters on Mars, makes Bosumtwi a remarkable impact structure on the African continent. An airborne radiometric survey of the southwestern part of Ghana reveals enigmatic circular feature enriched in potassium, coinciding with the crater rim and an outer ejecta ridge at Bosumtwi. The goal of this study is to investigate possible origins of these features, by impact processes (shock metamorphic effects, impact-induced hydrothermal systems) or postimpact surficial processes (erosion, weathering). The origin of these features is discussed here based on field observations, ground-based radiometric measurements, and first cosmogenic nuclide analyses (^{10}Be). The data indicate that the rim and outer ridge were eroded more rapidly than the rest of the impact structure. Accordingly, the downward advance of the weathering fronts in the annular moat, after ejecta emplacement, are responsible for leaching of K from the lateritic residual observed at the surface. The Bosumtwi impact structure is, therefore, a valuable natural laboratory to investigate the factors controlling erosion and weathering processes in the Ashanti belt since impact 1 Ma ago. Simulations of vertical profiles of ^{10}Be concentration further constrain local variations of the erosion rate. In light of this study, circular K anomalies in radiometric surveys might be indicative of potential impact structures in tropical regions.

INTRODUCTION

The Bosumtwi impact structure is located at 6°30'N/1°25'W in the Ashanti belt of Ghana, which is one of the major gold provinces in the world (Goldfarb et al., 2017). Bosumtwi is located in the Ghanaian part of the West African Craton. The structure (Fig. 1) is one of the best preserved impact structures in Africa (Gottwald et al., 2020; Reimold & Koeberl, 2014). Bosumtwi is one of the youngest impact structures

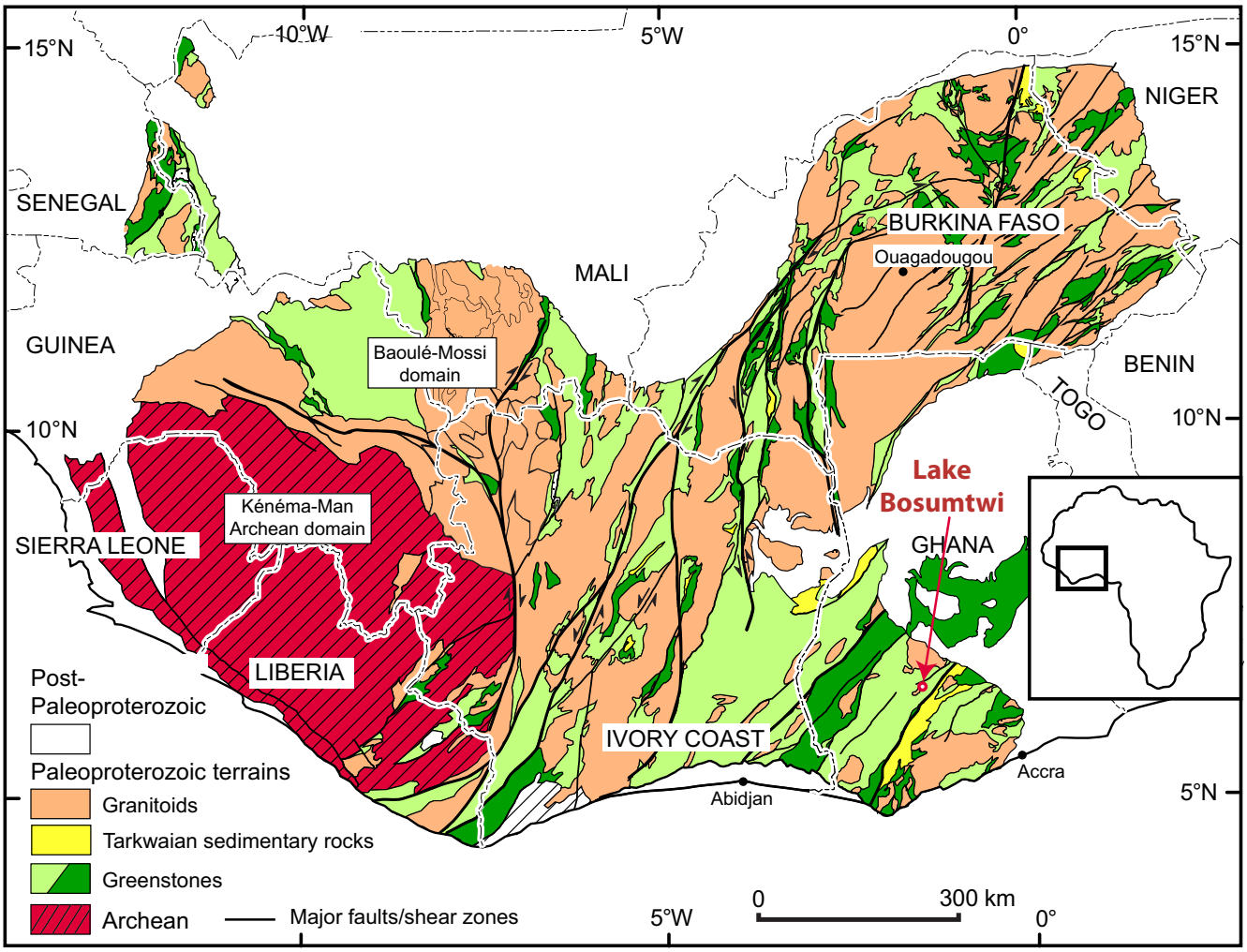

Fig. 1. Geological map of the West African Craton with the location of Lake Bosumtwi in the Paleoproterozoic metasedimentary rocks and greenstone belts of Ghana (after Milési et al., 2004). Cylindrical projection. (Color figure can be viewed at wileyonlinelibrary.com.)

known in Africa, with an age of 1.07 Ma (Koeberl et al., 1997), after the Kalkkop (0.25 ± 0.05 Ma) and Tswaing craters (0.220 ± 0.052 Ma) in South Africa. With a rim-to-rim diameter of 10.5 km (Fig. 2), Bosumtwi is a complex impact crater (Koeberl & Reimold, 2005; Koeberl et al., 1998). A major part of the structure's interior is obscured by water and sediment deposits of Lake Bosumtwi. The structure has a prominent crater rim that is elevated by up to 300 m above the crater lake and by 150–200 m above the environs of the crater. The crater rim is surrounded by an annular plateau, which is, in turn, surrounded by an outer ridge at 18 km from the center of the structure.

Two recent, independent studies have presented evidence that the annular plateau and outer ridge (Fig. 2) beyond the crater rim correspond to the ejecta deposits of the crater (Baratoux, Niang, et al., 2019; Wulf et al., 2019) that still comprise suevite deposits (e.g., Koeberl & Reimold, 2005). This interpretation is based on remote sensing and geomorphological analyses, including landform evolution modeling (Wulf et al., 2019), geophysical surveys, and field observations (Baratoux, Niang, et al., 2019). The morphology of the ejecta deposits is well preserved owing to the young age of the impact structure and to the low denudation rates observed at the regional scale (Beauvais & Chardon, 2013). Indeed, Baratoux, Niang et al. (2019) and Wulf et al. (2019) confirmed that the outer ridge, already reported in previous works (Jones et al., 1981; Wagner et al., 2002), represents a subtle topographic feature (a few tens of meters in elevation) that is directly inherited from ejecta emplacement as a surface flow. This morphology is similar to that of the ejecta of Martian rampart craters, interpreted to be the consequence of

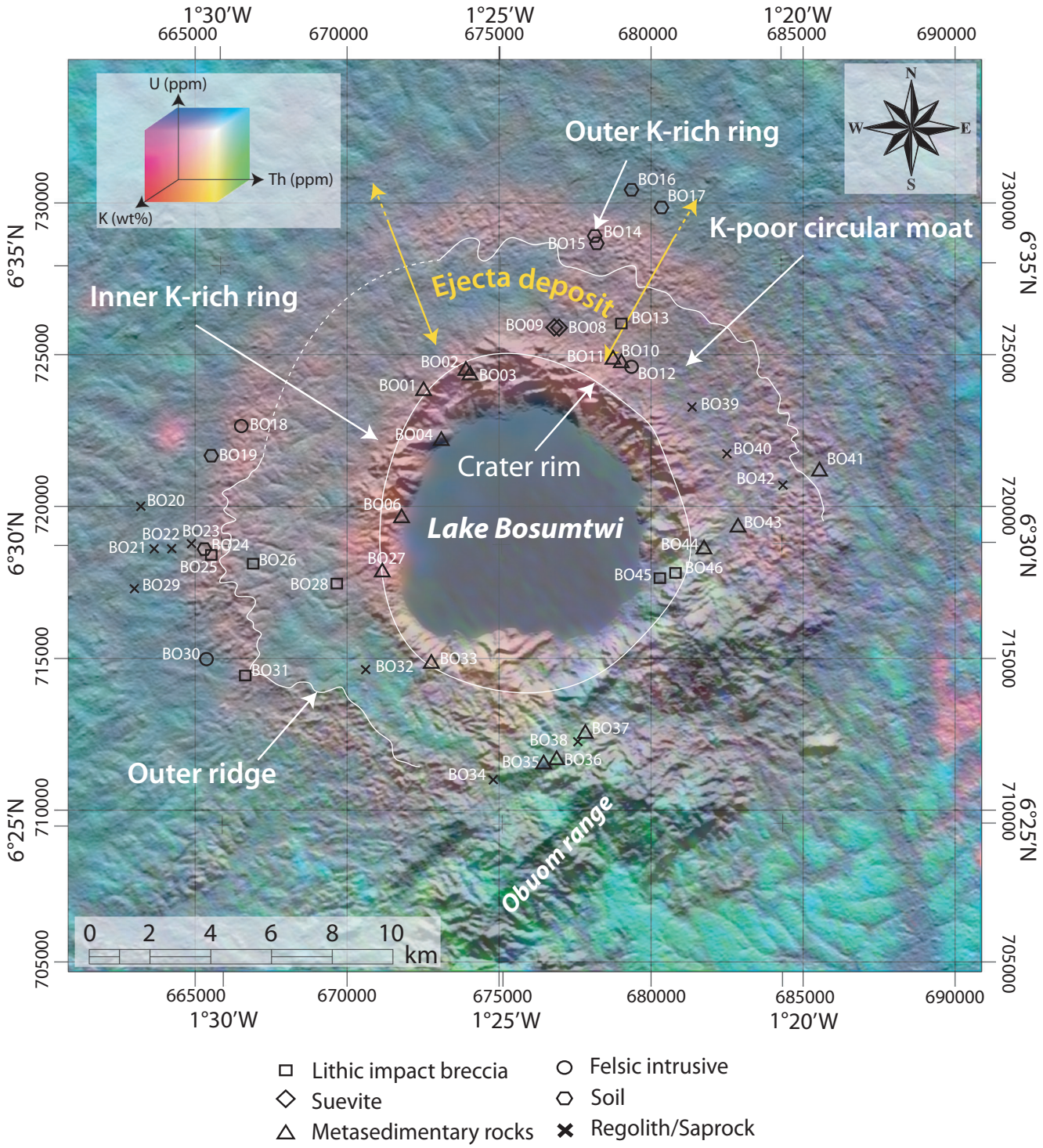

Fig. 2. Potassium, Th, and U concentration map in ternary RGB representation superposed onto the shaded relief image of the Bosumtwi impact structure (see Baratoux, Niang, et al. (2019) for the source of data and regarding data processing). Potassium (K): 0–2.5 wt% (red channel), Th: 0–9 ppm (green channel), U: 0–4 ppm (blue channel). Map projection UTM zone 30N, upper left coordinate: 660872.393E (1°32′41.06″W), 734674.385N (6°38′41.36″N), lower right coordinate 690842.393E (1°16′22.60″W), 704705.385N (6°22′22.60″N). The map illustrates the different components of the impact structure (crater rim, erosional remnants of the ejecta deposits, and its outer ridge), the location of the circular features enriched or depleted in K, the outer K-rich ring located near the outer ridge, the K-poor region corresponding to a circular depression (moat) within the ejecta deposits, and the inner K-rich ring corresponding to the crater rim. (Color figure can be viewed at wileyonlinelibrary.com.)

the incorporation of subsurface volatiles, responsible for a fluidized emplacement (Baloga, 2005; Barlow et al., 2000). Bosumtwi and the 15 Ma old Ries impact structure in Germany (Sturm et al., 2013) are the two first terrestrial impact structures for which this lobate ejecta morphology has been recognized. However, a recent study (Wulf et al., 2019) suggests that this ejecta morphology may be more commonly found at terrestrial impact craters over a wide range of crater sizes, but that it has been rarely preserved as well as in the cases of Ries and Bosumtwi.

The crater rim and ejecta deposits of Bosumtwi are also characterized by a peculiar geochemical feature that was revealed by regional airborne radiometric mapping (Boamah & Koeberl, 2002; Pesonen et al., 2003). This technique, which relies on the natural emission of gamma rays from the radioactive decay of ^{40}K, ^{232}Th, and ^{238}U, is commonly used for geological mapping and mineral exploration. It produces maps of potassium (K), thorium (Th), and uranium (U) concentrations in near-surface material (e.g., Wilford et al., 1997). The anomaly observed at Bosumtwi may be described qualitatively as a double ring enriched in K relative to the surrounding material (Fig. 2). This figure presents a radiometric map of the Bosumtwi impact structure, resulting from a combination of two intercalibrated radiometric surveys provided by the Geological Survey of Ghana (see Baratoux, Niang, et al. (2019) for details regarding data processing). The K-rich (1.5–2.5 wt%) regions are spatially correlated with the crater rim and with the outer ridge—both of which are considered the erosional remnants of the ejecta deposits. In contrast, K-poor areas (0.5–1.5 wt%) are found beyond the outer ridge and within an annular depression (or moat) between the crater rim and the outer ridge (Fig. 2). No such features have been reported for the Th and U concentrations (see Baratoux, Niang, et al., 2019) (Fig. 2). To confirm this observation by quantitative analyses, the frequency distribution of K, Th, and U within the rim, moat, and outer ridge areas, and around the crater have been estimated (Fig. 3). This clearly indicates that the rim and outer ridge are enriched in K with respect to the surrounding terrain. The K content in the moat appears to be intermediate between the rim and surrounding terrains. The U and Th frequency distributions are similar for all categories, with the exception of slightly elevated Th concentrations for the material outside the crater and its ejecta.

The origin of this surface geochemical signature was previously discussed by Boamah and Koeberl (2002), but essentially remained unresolved. These authors examined soil geochemistry and concluded that the enrichment in K "may reflect K mobilization due to the impact event, or source rocks with variable concentrations of K". In contrast, Baratoux, Niang, et al. (2019) suggested that this feature was mainly a reflection of the spatial distribution of surface exposures of fresh rock versus weathered material, the latter being depleted in K. According to this interpretation, the ring anomalies would have been developed since the impact event.

Under tropical climate, superficial materials probed by radiometric surveys are often composed of soil and regolith, covered by dense vegetation. The regolith is defined as "the weathered and transported blanket of material covering fresh rock. It may be defined as the entire unconsolidated and secondarily recemented cover that overlies more coherent bedrock, which has been formed by weathering, erosion, transport, and/or deposition of older material. Regolith includes fractured and weathered basement rocks, saprolite/saprock, soils, organic accumulations, glacial deposits, colluvium, alluvium, evaporites, aeolian deposits, and other sediments" (Anand & Butt, 2010). During in-situ measurement, the soil - the upper layer a few centimeters to a few tens of centimenters thick dominated by organic material - was classified. At Bosumtwi, this corresponds to black to brownish soil rich in organic materials. Soil and dense vegetation reduce the gamma ray signals, and well-developed alteration profiles depleted in mobile elements may often mask the chemical composition of the underlying fresh rock. Therefore, the interpretation of airborne radiometric data in terms of surface geology is not trivial. Determining the nature of the material enriched in K at Bosumtwi is, thus, critical to the understanding of the origin of the observed K-rich ring pattern. The objective of the present study is to address the following questions: What is the nature of the material enriched in K and what is the source of the K: soil, regolith, or the occurrence of certain rock types? How and when did these K-rich anomalies form? What is the possible significance of such a geochemical feature for impact science and what are the implications for weathering and erosion in the economically important Ashanti belt, since the impact event at 1 Ma?

The next section summarizes the geological setting of the Bosumtwi impact structure. It is followed (see the Methodology section) by a description of the methods implemented to elucidate the origin of the K anomaly, including (1) the compilation of geochemical analyses of regolith, and various rocks that were affected by the impact event, to build a geochemical baseline for addressing the question of the potential contributions of the various lithologies within the impact structure to the K-rich signature; (2) field observations and field mapping of K-rich and K-poor areas, as identified in the airborne survey; (3) ground-based measurements with a handheld

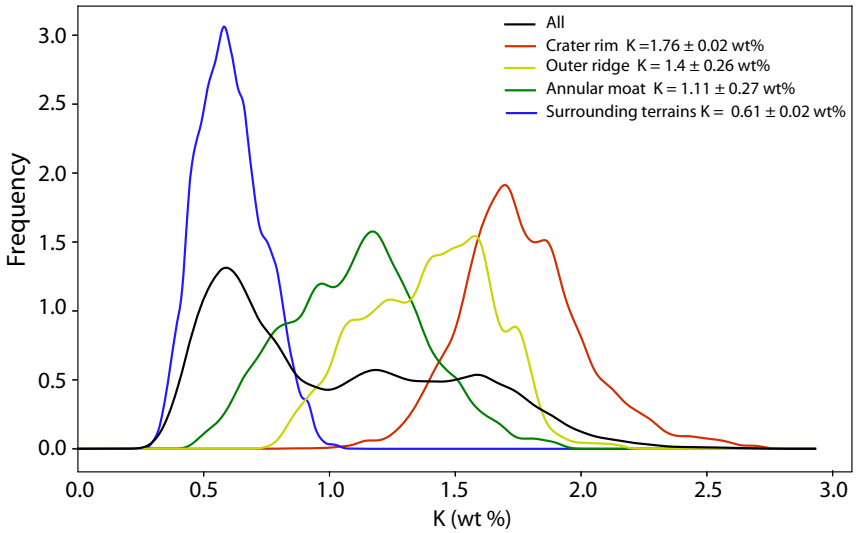

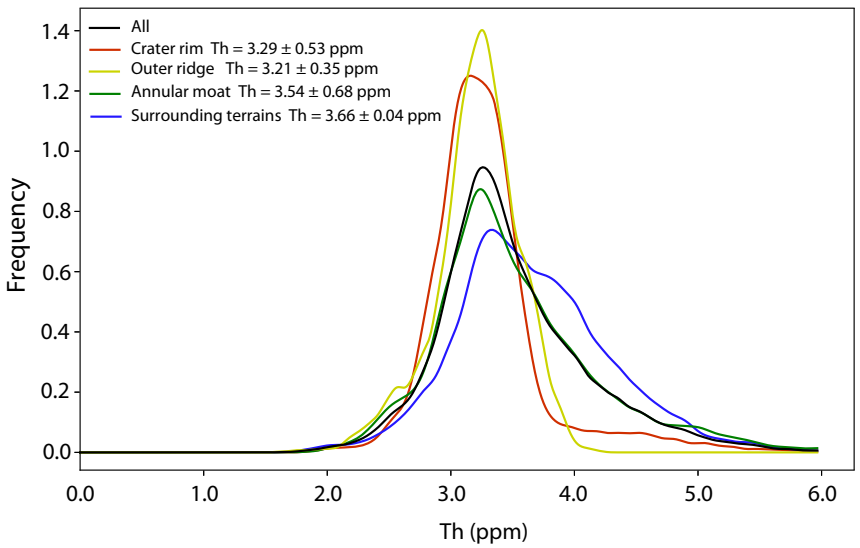

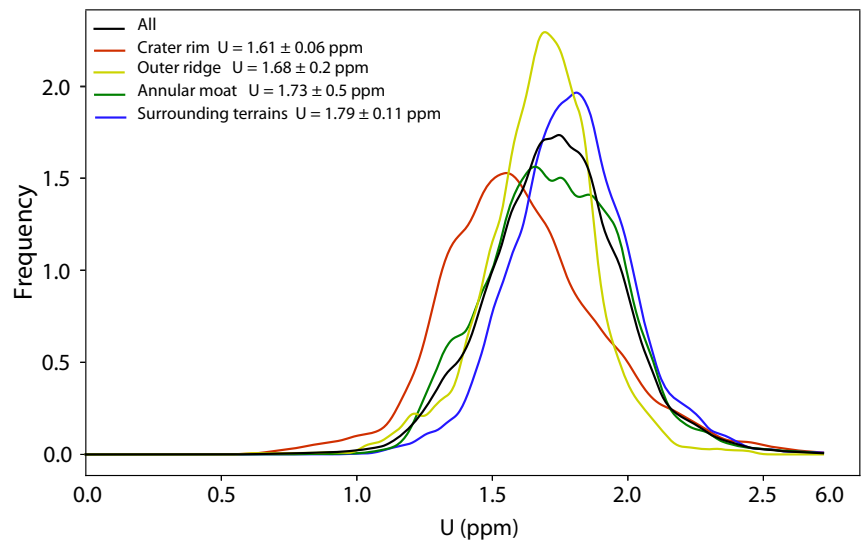

Fig. 3. Frequency distributions of K, Th, and U concentrations for the different locations in the crater structure, based on the radiometric map (compare Fig. 2). Average values and standard deviations for K (wt%) are 1.76 ± 0.02, 1.11 ± 0.27, 1.4 ± 0.26 and 1.4 ± 0.26 for the crater rim, annular moat, and the outer ridge areas, and the region surrounding the crater, respectively. Average values and standard deviations for Th (ppm) are 3.29 ± 0.53, 3.54 ± 0.68, 3.21 ± 0.35, and 3.66 ± 0.04 for the crater rim, the annular moat, the outer ridge, and the region surrounding the crater structure, respectively. Average values and standard deviations for U are 1.61 ± 0.06, 1.73 ± 0.25, 1.68 ± 0.2, and 1.79 ± 0.11 for the crater rim, the annular moat, the outer ridge, and the region surrounding the crater, respectively. (Color figure can be viewed at wileyonlinelibrary.com.)

spectroradiometer; and (4) cosmogenic nuclide (^{10}Be) measurements in near-surface material and on core samples from shallow bore holes within the ejecta deposits, to constrain exposure ages and/or erosion rates. The observations and results of each of these approaches are then presented (see the Results section). In the Discussion section, we analyze the results against the two different families of hypotheses of formation of this K anomaly, i.e., the mobilization and redistribution of K by the impact event, or by postimpact processes. This latter part includes the potential development of an impact-generated hydrothermal system, and the redistribution of K by superficial processes. A chronological model of formation of the circular pattern of K concentrations supported by our observations is then presented. The model is followed by recommendations and sampling strategies for further testing of our conclusions.

GEOLOGICAL SETTING AND GEOCHEMICAL BASELINE FOR THE TARGET ROCKS

Detailed geological descriptions of the Bosumtwi impact structure and its surroundings are given by Boamah and Koeberl (2003) and Koeberl and Reimold (2005). The Bosumtwi impact structure was excavated in lower greenschist-facies metasedimentary rocks of the 2.1–2.2 Ga Birimian Supergroup (Leube et al., 1990; Wright et al., 1985). The Birimian Supergroup consists of an assemblage of metasedimentary/volcanic rocks, including phyllites, metatuffs, metagraywackes, quartzitic metagraywackes, shales, and slates (Koeberl & Reimold, 2005). At Bosumtwi, Birimian metavolcanic rocks crop out only at the southeast of the structure. Tarkwaian clastic sedimentary rocks, which are regarded as detrital sediments after Birimian rocks (Leube et al., 1990), are exposed farther east and southeast of the Birimian metavolcanic unit. The hills occurring to the southeast of the structure, named "the Obuom Range," are mainly composed of Birimian metavolcanics and metasedimentary rocks, with minor basic intrusives. Proterozoic granitic intrusions have also been mapped within the structure. Two families of dikes of dolerite and amphibolite have been noted around the crater (see Fig. 4, minor intrusives, green color). The N–S trending dikes have an age of 867 ± 16 Ma and the dike family oriented NE–SW has an age of 915 ± 8 Ma (Baratoux, Söderlund et al., 2019). In the immediate environs of the crater, the lithology is dominated by metagreywacke, sandstone/quartzitic rocks, and minor mica schist. Proterozoic granitic intrusions, weathered granitoid dikes, and dolerite and amphibolite dikes are also present in the region around the crater (Junner, 1937; Koeberl & Reimold, 2005; Moon & Mason, 1967; Woodfield, 1966). Recent rock formations include the Bosumtwi lake beds, as well as soils and breccias associated with the formation of the crater (Jones, 1985; Jones et al., 1981; Junner, 1937; Koeberl et al., 1997, 1998; Kolbe et al., 1967; Moon & Mason, 1967). Suevite exposures have been observed just outside the northern and southwestern crater rim (Fig. 4). On the basis of composition and texture, Boamah and Koeberl (2003) distinguished three types of impact breccia at the Bosumtwi crater: an autochthonous monomict lithic breccia that occurs on the northern part of the crater rim, a probably allochthonous polymict lithic impact breccia (also to the north of the crater rim), and a suevitic breccia. The suevitic breccia was identified in two main areas only, to the north and to the south of the crater, about 1 km outside of the crater rim. This breccia contains impact melt fragments and a variety of country rock clasts, including metagraywacke, phyllite, shale, and granite clasts of up to about 40 cm size.

A series of boreholes was drilled in 2004 in the central area of the crater lake within a project sponsored by the International Continental Scientific Drilling Program (ICDP) (Koeberl et al., 2007). Two of these holes (LB-07A and LB-08A) allowed detailed investigation of the impact breccia fill (Coney et al., 2007; Ferrière et al., 2007, 2010). The petrography of rocks from these two boreholes indicates that the central uplift of the impact structure is composed of brecciated Birimian metasedimentary rocks and impact melt-poor polymict impact breccia (Ferriere et al., 2008).

METHODOLOGY

The Geochemical Database

To support the investigation of the airborne radiometric survey, we built a database of all available geochemical analyses of rocks and soils of the Bosumtwi area (Table S1 in supporting information). This database

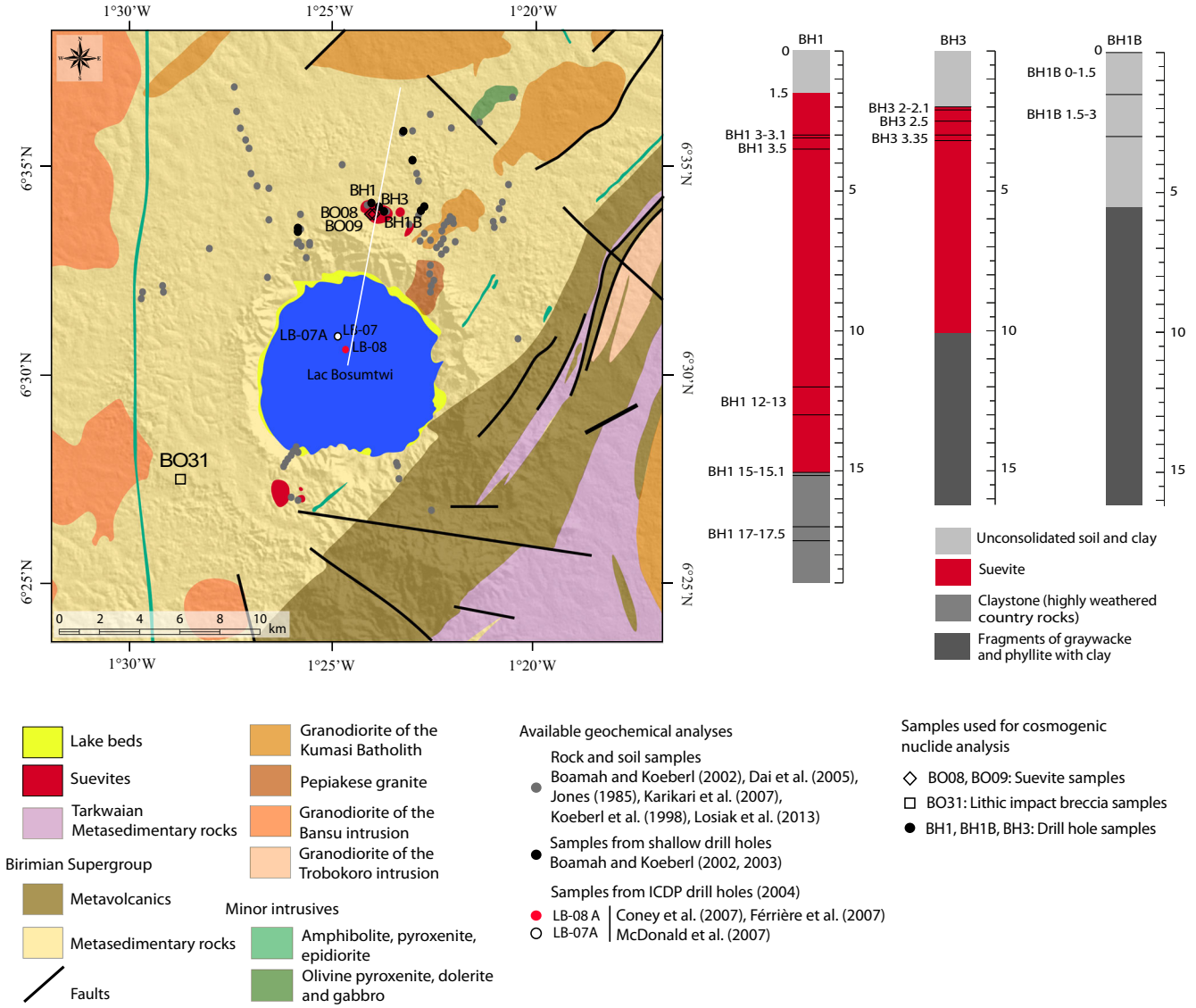

Fig. 4. Geological map of the Bosumtwi impact structure, modified after Koeberl and Reimold (2005) and Baratoux, Niang, et al. (2019), with locations of samples of available geochemical analyses, surface samples (BO08, BO09, and BO31, this work), and samples from the shallow boreholes (BH1 and BH3), which were used for cosmogenic nuclide analysis. The white line is a radial profile crossing BH1 (see Fig. 16). Map projection UTM zone 30N, as in Fig. 2. (Color figure can be viewed at wileyonlinelibrary.com.)

allows investigation of the diversity of K, Th, and U concentrations of the different lithologies, regolith, and soils. The geochemical analyses (major and trace elements) were extracted from various publications of the last four decades (Boamah & Koeberl, 2002; Coney et al., 2007; Dai et al., 2005; Ferrière et al., 2007, 2010; Jones, 1985; Karikari et al., 2007; Koeberl et al., 1997, 1998; Losiak et al., 2013; McDonald et al., 2007) (see Fig. 4 for sample locations). Five categories of lithology, which represent the main potential contributions to the airborne radiometric signatures, are distinguished: lithic impact breccias (either monomict or polymict), suevites (this category also includes a few analyses of melt particles), metasedimentary rocks, felsic intrusives, regolith (lateritic soil), and tektites.

Field Observations and In Situ Measurements of K, Th, and U Concentrations

Field work carried out in November 2017 involved observations at outcrops and ground measurements of K, Th, and U concentrations using a handheld field gamma ray spectrometer of the type RS-BGO 230 (denoted hereafter FPGRS, for field portable gamma ray spectrometer). The crater area is accessible along roads and tracks, even where the forest is dense.

Measurement sites were chosen on the rim, in the moat, and along the outer ridge, according to accessibility and presence of outcrops. Thus, 233 measurements of K, Th, and U concentrations of rocks, regolith, and soil (black-brownish unit of a few cm rich in organic matter) were collected at 46 sites within the impact structure (locations of ground measurements are shown in Fig. 6.). The measurements were done in the form of multiple spot analyses, whereby the integrated volume (~1 m^3) assessed by this technique was always larger than sizes of typical rock samples. The accuracy and precision of this technique, the influences of the conditions of measurements (temperature, outcrop geometry), and the scale factors when comparing K, Th, and U concentrations obtained with different methods have been addressed in previous publications (Baratoux et al., 2014; Fall et al., 2018, 2020). Based on these experiences, an acquisition time of 3 min per measurement was selected, which yields an accuracy of about 0.1 wt% for K, 0.5 ppm for Th, and 1 ppm for U (Baratoux et al., 2014). This accuracy is lower than that obtained in laboratory measurements, but is sufficient to discriminate the different types of material encountered at Bosumtwi. The lower accuracy is also compensated by the large number of analyses and the scale of each analysis (typically 1 m^3), whereas accurate concentrations of chemical elements measured in the laboratory for an individual sample of a few hundred grams are not necessarily representative at the outcrop scale (Fall et al., 2018). The compilations of available geochemical data and of in situ determinations of K, Th, U concentrations are therefore complementary approaches that, together, are relevant to our scientific questions. Observations and measurements were achieved in the different geological units, within the different structural zones of the impact structure (rim, moat, and outer ridge of the ejecta deposits, and outside of the ejecta deposits), as well as in areas representative of both high and low K concentrations, according to the airborne survey. For each outcrop and each measurement, the lithology was noted and classified into one of these five groups: metasedimentary rocks, felsic intrusives, lithic impact breccias, suevites, and regolith. Several stops in places with no rock exposures were made to obtain K, Th, and U concentration values for soils in areas of high and low K concentrations according to the airborne survey.

Cosmogenic Nuclide Measurements

Cosmogenic nuclides, including ^{26}Al and ^{10}Be, are produced in the atmosphere and at the surface (in situ) by spallation reactions, negative muon capture, and/or thermal neutron capture during interaction of terrestrial material with cosmic rays (Dunai, 2010). Cosmogenic nuclides ^{10}Be and ^{26}Al offer various applications in geosciences and are particularly used in geomorphology (exposure age and denudation rates), given their half-lives of, respectively, 1.387 ± 0.012 Ma for ^{10}Be (Chmeleff et al., 2010; Korschinek et al., 2010) and 708 ± 17 ka for ^{26}Al (Nishiizumi, 2004). Cosmogenic nuclides have also been used to trace the surface origin of clasts displaced during the impact process (Losiak et al., 2014).

In situ production of the cosmogenic nuclides ^{10}Be and ^{26}Al occurs in rocks and minerals exposed at surface and then decreases exponentially with depth. The production rate at 1 m depth is, for instance, only 20 % of the surface rate. From the concentrations of these isotopes, one can either determine an exposure age or a long-term (thousands to hundreds of thousands of years) denudation rate, considering a steadily eroding landscape (Brown et al., 1995; Granger et al., 1996). This approach is potentially useful to document the local variation of denudation rates at the Bosumtwi impact crater since its formation.

Fifteen samples were analyzed here for ^{10}Be and ^{26}Al, three from the field campaign of November 2017 and the rest from drill cores of the shallow bore holes achieved in 1999 by the University of Vienna (Boamah & Koeberl, 2003). The locations and depths of the samples are presented in Fig. 3. The uncertainties on sample depths are large and not ideal for a cosmogenic nuclide study. This current limitation shall be addressed by future field investigation dedicated to consolidate these preliminary results. Drill holes BH1, BH1B, and BH3 have maximum depths of 30 m (Boamah & Koeberl, 2006). The drill holes are composed—from bottom to top—of claystone (a product of strong weathering of country rock), suevite, and soil (BH1); fragments of greywacke and phyllite with clay, suevite, and soil (BH3); and fragments of greywacke and phyllite with clay and soil (BH1B) (Fig. 3). Samples collected during the field campaign are labelled BO08, BO09, and BO31. Both BO08 and BO09 were sourced in the northern part of the Bosumtwi structure and are near-surface samples that consist of altered suevite with generally devitrified melt particles. Sample BO31 represents a polymict lithic impact breccia collected to the southwest of the crater structure (see Fig. 4 for the locations of these samples).

Samples were prepared at CEREGE–Aix-en-Provence, following standard methodology. Each sample was crushed and sieved (between 0.25 and 1 mm) and approximately 200 g of material was recovered (20 g per sample). This mass was subjected to Frantz magnetic separation. The extraction of pure quartz was done by several leachings in a HCl

(hydrochloric acid) and H_2SiF_6 (hexafluorosilicic acid) mixture (both Normapur quality) for 48 h, whereby the solutions were changed after 24 h of shaking.

Atmospheric ^{10}Be was then removed by a series of three sequential dissolutions with HF (Normapur 48 %). After cleaning with ultrapure water (18 MOhms), ~20 g of quartz was spiked with 0.15 mg of a 3025 ppm ^{9}Be solution and then totally dissolved in HF. This latter solution was evaporated and the remaining precipitate was recovered with 1 M nitric acid. An aliquot of 0.2 mg was collected to measure the amount of natural ^{27}Al by ICP-OES using a Thermo ICAP6500. Beryllium was then extracted using cationic and anionic resin exchanges. Beryllium hydroxides were heated at 800 °C for 1 h. The resulting BeO was mixed with metal powder (niobium) and then pressed into copper cathodes prior to measurements on ASTER, the French Accelerator Mass Spectrometer (Cerege, Aix-en-Provence). Beryllium data were calibrated directly against the STD11 standard (Braucher et al., 2015) with a $^{10}Be/^{9}Be$ ratio of $1.191 \pm 0.013 \cdot 10^{-11}$. Due to difficulties encountered during quartz purification and despite having planned to also measure ^{26}Al, the results on the latter nuclide will not be presented here, as the ^{27}Al concentrations were far too high (from 200 ppm up to 17,000 ppm) to allow an accurate AMS (accelerator mass spectrometry) measurement (bad counting statistics and ratios at the level or below the $^{26}Al/^{27}Al$ ratio) of ^{26}Al.

RESULTS

Analysis of the Geochemical Database

The analysis of the geochemical database provided in the supporting information is focused on the frequency distributions of K, Th, and U concentrations in the different litho-categories (lithic impact breccias, suevites, metasedimentary rocks, felsic intrusive, regolith) (Fig. 5). These categories represent possible contributions to the geochemical composition of surface material. The frequency distributions of K, Th, and U concentrations of tektites are also examined, as these objects also provide insights into the composition of surface material present at the time of impact. Ivory Coast tektites (Ivoirites) have narrow distributions of concentrations of K, Th, and U, reflecting their generally homogenous chemical composition (Koeberl et al., 1998). Suevites also have unimodal distributions of K, Th, and U concentrations, with peaks at K = 1.3 wt%, Th = 3.1 ppm, and U = 1 ppm, respectively. The lithic impact breccias have a wide range of K concentrations (from ~0.5 to 2.5 wt%, with a peak at 1.8 wt%). The distributions of Th and U concentrations are unimodal, with peaks at ~3 ppm and 1 ppm, respectively. Felsic intrusive rocks have a bimodal distribution of K, Th, and U concentrations, with a major peak at K = 1.4 wt%, Th = 3.2 ppm, and U = 1 ppm, and a minor peak at K = 3.6 wt%, Th = 0.9 ppm, and U = 3.6 ppm. Metasedimentary rocks have bimodal distributions for K and Th, with a primary peak at K = 0.9 wt% and Th = 3 ppm and a secondary peak at K = 2.1 wt% and Th = 4.1 ppm. The distribution of U is unimodal with a peak for U = 1 ppm. Regolith is characterized by a wide range of concentrations in K, with the distribution being dominated by low values. The distributions of the K, Th, and U concentrations in various types of material do not offer a straightforward explanation for the origin of the annular pattern of K surface concentrations. Thorium and U are not useful to discriminate the different lithologies, as the distributions of concentrations for the different lithological groupings overlap. K-rich felsic intrusive rocks may contribute to K-rich areas at the surface, but the volume of excavated felsic intrusive with respect to that of metasedimentary rocks seems to have been small, and it is difficult to conceive how felsic intrusive rocks would form a circular pattern following excavation and ejecta emplacement, considering the plausible pre-existing geometries of felsic intrusions at depth (discontinuous plutons).

An interesting observation is the distribution of K in metasedimentary rocks. These rocks include sandstones, metagraywackes, mica-schists, and shales, and are more or less weathered. Though they were not systematically classified into subcategories, we explored the relation between K with a few other selected elements (Th, U, Al, and Si) and as a function of depth (Fig. 6). We also calculated Pearson coefficient values, which allow a linear correlation between variables (K and other elements, and are always <1). The relation between K with Th, U, Al, and Si suggests that the variation of K concentrations is mostly controlled by the nature of the metasedimentary rock and, in particular, by the relative proportions of sandstone/claystone in the protolith. Indeed, the concentration of K is not correlated with depth (see Fig. 5), but is

Fig. 5. Frequency distributions of K, Th, and U concentrations, based on the geochemical database for Bosumtwi surface and drill core samples (see supporting information), for five different lithological types (lithic breccia, suevites, metasedimentary rocks, felsic intrusive, regolith), and Ivory Coast tektites. Dotted vertical lines indicate the range of variations of K, Th, and U concentrations on the ejecta deposits and crater rims based on airborne radiometric data. (Color figure can be viewed at wileyonlinelibrary.com.)

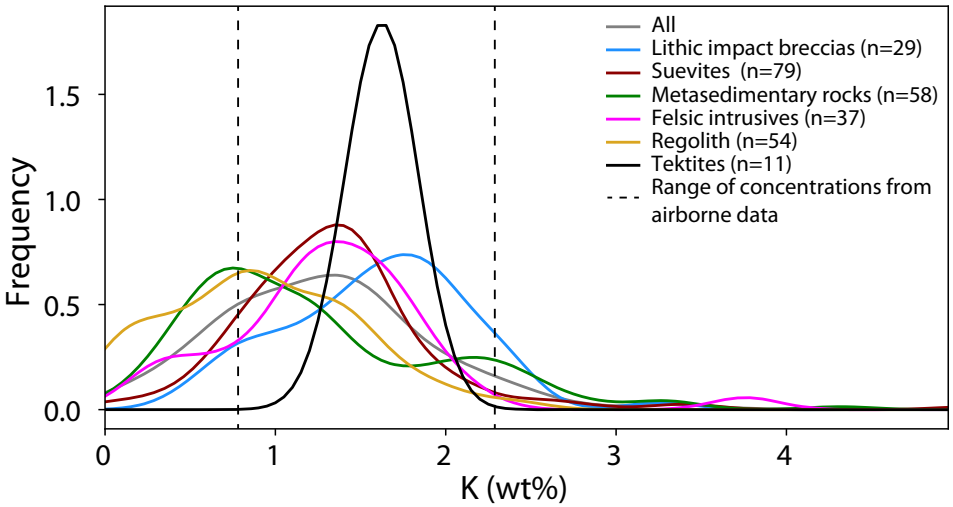

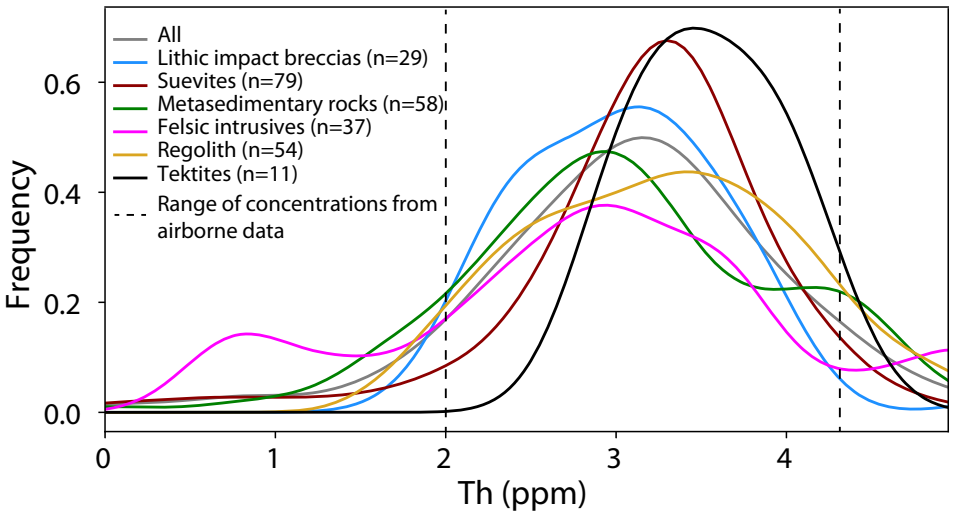

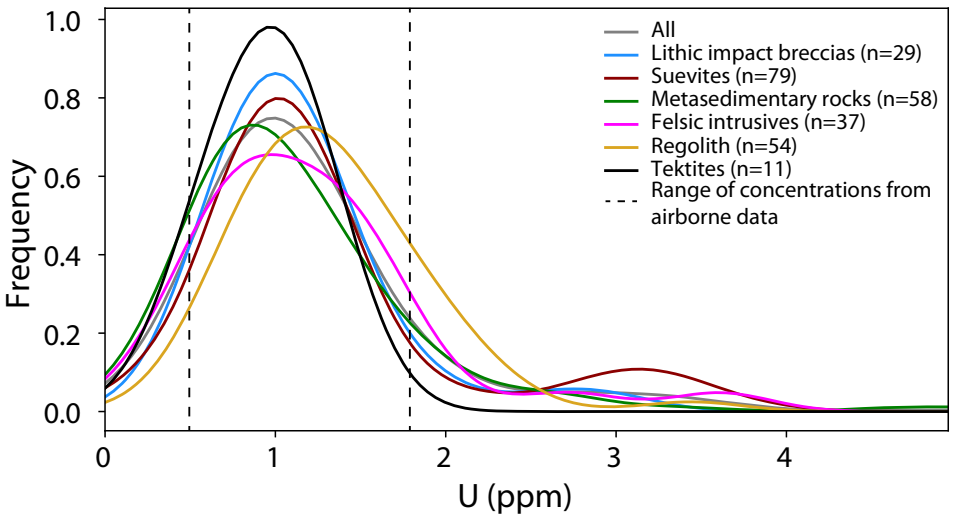

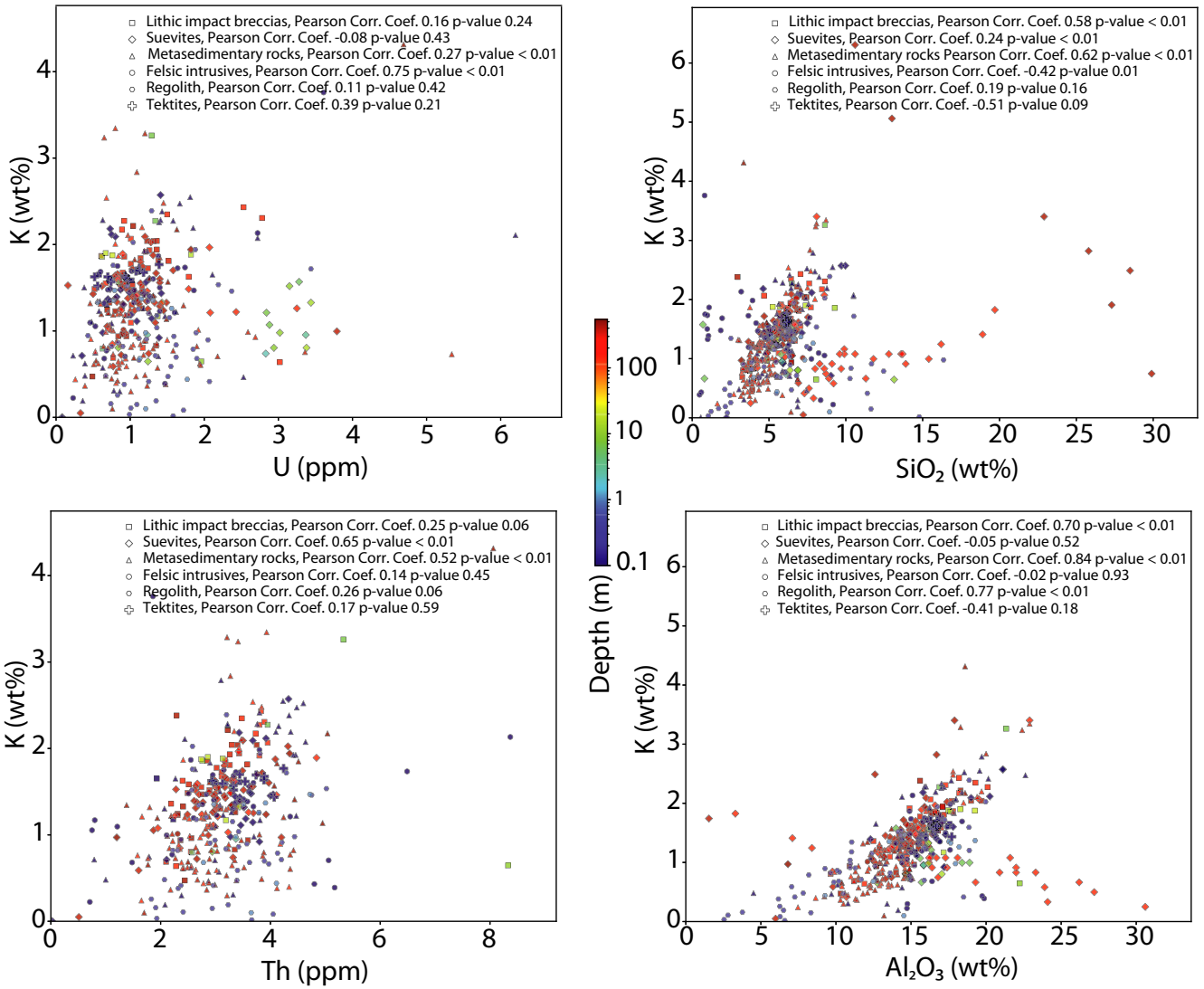

Fig. 6. Plots of the abundances of K versus Th, Al_2O_3, and U, and of U versus Th concentrations for the different lithological categories (lithic impact breccias, suevites, metasedimentary rocks, felsic intrusives, regolith), and Ivory Coast tektites of the Bosumtwi geochemical database. (Color figure can be viewed at wileyonlinelibrary.com.)

somewhat correlated with Al (Pearson correlation coefficient of 0.84, with $P < 0.01$).

Field Observations

The locations of field observations are shown in Fig. 2. Forty-six sites of rocks, regolith, and soil within the impact crater, across the two circular K anomalies, one coinciding with the actual crater rim (ca. 11 km diameter), and the other one marking the outer ring anomaly (ca. 18 km diameter), and outside the crater were visited and K, Th, and U concentrations were measured. The Bosumtwi area is characterized by a well-developed and thick regolith on a regional scale which is typical at these latitudes. Lithologies encountered are mainly composed of metasedimentary rocks (schists, slates, metagraywackes, and quartzites), highly altered granitic bodies, and some suevite and lithic impact breccias. The respective lithologies observed are also presented in the same five lithotypes, for intercomparison with the other sources of data. Good agreement was found between our observations and the geological map of Koeberl and Reimold (2005), with the exception of an exposure of a felsic intrusive at BO18, in addition to the suevite exposed at the locality B009. Several granite bodies, mostly microgranitic, were encountered adjacent to the crater rim and near the ejecta ridge. These bodies are strongly weathered (Fig. 7).

An outcrop of metavolcanic rock was recorded on the eastern side of Bosumtwi. Outcrops of lithic impact

Fig. 7. Outcrop pictures of K-rich metasedimentary rocks exposed on the top of the crater rim. a) Outcrop BO01 (6°32.44'N/1°26.23' W), and (b) outcrop BO27 (6°29.29'N/1°27.6' W), associated with elevated concentrations of K (2–3 wt%); pen (10 cm long) and portable gamma-ray spectrometer RS-230-BGO (26 cm long) for scale. c) Outcrop BO31 (6°27.38'N/1°29.34' W), lithic breccia exposed on surface. The location of this outcrop is indicated in Fig. 2. (Color figure can be viewed at wileyonlinelibrary.com.)

breccia from metasedimentary rocks were exclusively found at the crater rim (either on the crest of the rim, or within 600 m from the crest, on the inner or outer flank of the crater rim), as well as near the outer ridge (Fig. 4). No rock exposures were found within the annular moat, which is generally covered by soil and vegetation, except for a few locations where regolith or saprock were observed (BO32, BO39, BO42) (Fig. 8a). Outcrops are rare beyond the outer ridge, where a thick lateritic cover occurs (Fig. 8b). These laterites can be thicker than 15 m in places, according to an observation at a road cut (see image in Fig. 8c and location of BO34 in Fig. 2).

In Situ Measurements of K, Th, and U Concentrations

The concentration map of Fig. 2 represents the in situ measurements of K, Th, and U concentrations (see

Fig. 8. Images of K-poor areas: (a) weathered metasedimentary rock (saprock) exposed on the surface, outcrop BO39 (6°32.25'N/1°21.35'W), 14 cm pen for scale. b) Lateritic cover outside of the outer ring anomaly, outcrop BO29 (6°29.10'N/1°31.33'W), portable gamma-ray spectrometer RS-230-BGO (26 cm long) for scale. c) Outcrop at location BO34 (6°25.47'N/1°25.9'W), outside the ejecta deposits and, therefore, beyond the outer ridge. Here, a thick lateritic cover is exposed in a road cut. This about 15 m thick lateritic cover is likely representative of the subsurface in the area surrounding the impact structure. The locations of these outcrops are indicated in Fig. 2. (Color figure can be viewed at wileyonlinelibrary.com.)

Table S2 in the supporting information) superimposed onto the ternary representation of the results from the airborne survey. First, in situ measurements were directly compared with values from the airborne survey (Pesonen et al., 2003). An area of 3*3 pixels (to minimize possible misregistration effects between the airborne survey and our in situ measurements) was extracted around each FPGRS measurement location and the average and standard deviations of K, Th, and U concentrations within this region of interest were recorded. The comparison of FPGRS measurements with airborne values is given in Fig. 9. Differences between in situ and airborne observations may result from the difference of the scale of measurements (~1 m for FPGRS data, about 200 m for the airborne survey), calibration issues, and measurement errors. Considering the large differences in scales between airborne and ground-based data, the main reason for the observed mismatch are likely short wavelength variations of K, Th, and U concentrations (Fall et al., 2018) associated with variable proportions of soil, regolith, and rock within each of the airborne survey pixels. When average values of K, Th, and U concentrations are considered for each type of material, the agreement between airborne and in situ measurements is better (Fig. 9, larger symbols, and Table 1), but some differences persist. For instance, the concentrations of K in metasedimentary rock and lithic breccia are higher for the in situ measurements than for the airborne survey. This difference may be readily explained if the 3*3 pixels region of interest is not exclusively composed of rocky outcrop but also includes soil and regolith cover. Despite these issues related to differences in scales, we consider that the in situ and airborne observations deliver a consistent message regarding the nature of K-poor (<1.5 wt%) and K-rich material (1.5–3 wt%): according to both approaches, K-poor material mainly corresponds to regolith, which is widely present within the annular moat and beyond the outer ridge. In contrast, K-rich material is represented by all other rock types, including metasedimentary rock, lithic breccia, and felsic intrusives. Surface exposures of K-

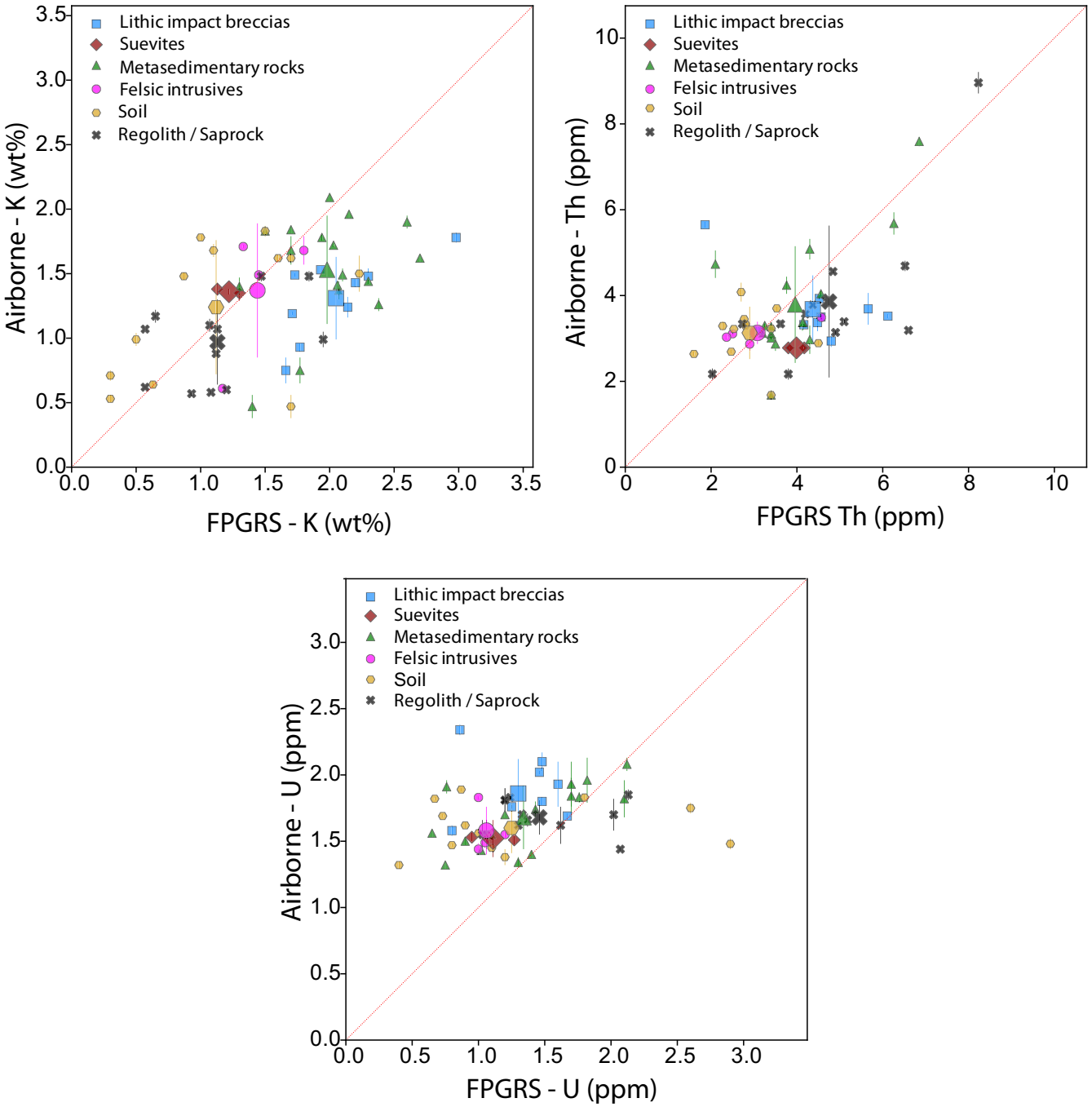

Fig. 9. Comparisons of K, Th, and U concentrations, at the same locations, from airborne radiometric data and FPRGS measurements. Airborne data are averaged within a square region of 3*3 pixels around the actual FPGRS measurement location. Larger symbols correspond to the average values for each lithology. (Color figure can be viewed at wileyonlinelibrary.com.)

rich materials are dominated by metasedimentary rocks and lithic breccias.

In conclusion, the nature of the K-poor and K-rich material forming an annular pattern in the airborne survey is clearly elucidated from field observations and FPGRS measurements. The K-poor material is composed of regolith, which occurs throughout the moat and outside of the impact structure. The K-rich material was measured on rocky exposures that are dominated by metasedimentary rocks and lithic impact breccias formed from metasedimentary rocks. These outcrops occur exclusively in two regions—between the

Table 1. Mean concentrations of K, Th, and U from in situ (this work) and airborne measurements (Pesonen et al., 2003) as a function of lithology. Note that standard deviations are often comparable or lower than the expected accuracy of each individual measurement. This means that the in situ measurements cannot discriminate between real variations of concentrations within a given lithological group and instrumental noise. However, even with the large error bars of in situ measurements, it is possible to discriminate between certain types of lithology, in particular, between regolith and fresh rocks.

	Airborne data			In situ measurements		
Lithology	K (wt%)	Th (ppm)	U (ppm)	K (wt%)	Th (ppm)	U (ppm)
Metasedimentary rocks	1.53 ± 0.42	3.79 ± 1.36	1.68 ± 0.24	1.98 ± 0.39	3.96 ± 1.14	1.34 ± 0.46
Felsic intrusives	1.37 ± 0.52	3.13 ± 0.26	1.58 ± 0.18	1.44 ± 0.27	3.08 ± 1.01	1.06 ± 0.09
Lithic impact breccias	1.31 ± 0.32	3.68 ± 0.79	1.86 ± 0.26	2.05 ± 0.42	4.37 ± 1.27	1.30 ± 0.32
Suevites	1.36 ± 0.02	2.78 ± 0.001	1.52 ± 0.14	1.22 ± 0.12	3.99 ± 0.26	1.11 ± 0.23
Regolith/saprock	0.97 ± 0.33	3.86 ± 1.77	1.68 ± 0.13	1.13 ± 0.45	4.75 ± 1.73	1.46 ± 0.40
Soil	1.24 ± 0.52	3.13 ± 0.61	1.60 ± 0.19	1.12 ± 0.63	2.9 ± 0.73	1.25 ± 0.78

crest of the crater rim and the distal ridge formed by ejecta deposits.

Cosmogenic Nuclide Study

The results of the cosmogenic nuclide study are given in Table 2. These concentrations are one to two orders of magnitude lower than those measured on tektites and in soil sediment in this region, either within the moat or beyond the ejecta deposits. This difference is easily explained, as Serefiddin et al. (2007) concluded from ^{10}Be concentrations in Ivory Coast tektites in soil samples (see Appendix for data) that high ^{10}Be concentrations could only have a meteoric origin, i.e., most of the measured ^{10}Be was made in the atmosphere (where the ^{10}Be production rate is much higher than on the ground) and then adsorbed at the surface of grains. Our lower ^{10}Be concentrations rather correspond to in situ production within minerals, as the meteoric component of our samples was removed by leaching of the surface of grains during chemical treatment.

DISCUSSION

Boamah and Koeberl (2002) suggested that the variations in the concentration of K may reflect either variable concentrations of K in the source rocks or soils, or mobilization of K as a direct consequence of the impact, due to redistribution of lithologies and/or hydrothermal overprint. These two hypotheses are evaluated first in the light of our new observations, in the section Variation of K Concentrations in the Target Rock and Removal of K from Impactites During the Impact Process sections, respectively. As neither of these two hypotheses appear to be compatible with our observations, we have explored a third hypothesis: the redistribution of K by postimpact superficial processes (regolith formation since the formation of the crater). We then propose a chronological model for the formation of the K surface patterns and discuss possible future investigations based on simulation of cosmogenic nuclide abundances in superficial material as a function of erosion rate.

Variation of K Concentrations in the Target Rock

The excavation flow and ballistic trajectories of ejecta can result in the transposition of vertical variations of the mineralogical or chemical composition into chemical or mineralogical lateral variations within ejecta deposits. Such variations in ejecta composition related to stratigraphy have been observed at Meteor Crater (Arizona) (Ramsey, 2002). The radial variations in the chemical composition of pyroxenes in the ejecta of several impact craters in the volcanic region of Syrtis Major on Mars have been related to the variation of pyroxene composition at depth (Baratoux et al., 2007). In the case of Bosumtwi, the geochemical database reveals a bi-modal distribution of K in metasedimentary rocks. The annular pattern might be the result of the excavation of alternating layers of K-rich and K-poor sediment. The variation of K concentrations as a function of the composition of metasedimentary rocks, as reported in the Geological Setting and Geochemical Baseline for the Target Rocks section for the "Bosumtwi geochemical database," does not appear to play a role in controlling the annular pattern of K concentrations. Furthermore, Fig. 10 shows the variation in K, Th, and U concentrations for the target rocks as a function of depth and invalidates this hypothesis. There is no systematic variation of K with depth that could be invoked to explain lateral variations in the concentration of K in the ejecta. Moreover, field observation shows that regions poor in K are not

Table 2. Results of AMS measurements of ^{10}Be contents in samples from the Bosumtwi impact structure, from this study (B008, B009, B031, BH1, and BH1B).

Depth (m)	Sample	Comment on location	Lithologies	^{9}Be (10^{19} at g^{-1})	Sample weight (g)	^{10}Be (kat g^{-1})	Max. erosion rate (m/Ma)
-	B008	Moat	Suevite	3.10	26.56	3442 ± 230	0.24 ± 0.02
-	B009	Moat	Suevite	3.09	6.91	88.5 ± 6	27.7 ± 1.87
-	B031	Outer ridge	Polymict lithic breccia	3.09	24.10	13.6 ± 1.1	196 ± 15.9
0.75 ± 0.75	BH1B-0-1.5	Moat	Regolith	3.10	27.19	184 ± 5.7	n.d.
0.75 ± 0.75	BH1B-0-1.5b	Moat	Regolith	3.16	5.94	153 ± 7.3	n.d.
2.05 ± 0.05	BH3-2.2.1	Moat	Suevite	3.11	2.16	179 ± 12.9	n.d.
2.5	BH3-2.5	Moat	Suevite	3.15	4.07	762 ± 69.9	
1.75 ± 0.75	BH1B-1.5-3	Moat	Regolith	3.17	36.02	115 ± 3.7	n.d.
1.75 ± 0.75	BH1B-1.5-3b	Moat	Regolith	3.12	12.35	74.4 ± 4.7	0.49 ± 0.04
3.05 ± 0.05	BH1-3-3.1	Moat	Suevite	3.12	5.08	434 ± 35	5.63 ± 0.27
3.35	BH3-3.35	Moat	Suevite	3.10	3.61	115 ± 13.5	5.46 ± 0.34
3.5	BH1-3.5	Moat	Suevite	3.17	6.13	508 ± 32.7	n.d.
12.5 ± 0.05	BH1-12-13	Moat	Suevite	3.12	23.52	62 ± 13.8	
15.05 ± 0.05	BH1-15-15.1	Moat	Regolith	3.12	3.25	127 ± 8.1	n.d.
17.25 ± 0.025	BH1-17-17.5	Moat	Regolith	3.11	5.38	270 ± 60.2	n.d.

associated with a particular type of target rock but with the local occurrence of regolith.

Removal of K From Impactites During the Impact Process

If variation of K concentrations in the locally occurring target rocks is not responsible for the observed distribution pattern of K at surface, the impact event itself may have induced modification of the K concentrations in impactites. Removal of volatile elements, such as H, C, and S, from impact melt, has been well-established (Tyburczy et al., 1986, 1990). Potassium is a less volatile element than these species, with a 50 % condensation temperature of 1006 K (Lodders, 2003). The giant Moon-forming impact has long been considered a possible explanation for the depletion of K in the lunar mantle, relative to the Earth's mantle (Ringwood, 1970). Removal of K in lunar regolith has been suggested based on isotopic studies on Apollo samples (Humayun & Clayton, 1995) and in the regolith of Vesta based on isotopic analyses of howardite-eucrite-diogenite meteorites (Tian et al., 2019). Volatile depletion in tektites involving vaporization of Cu, Zn, and K was reported by Jiang et al. (2019). Potassium loss in rocks has been produced experimentally (Lambert & MacKinnon, 1984). These authors reported K loss in micas of experimentally shocked gneiss and demonstrated that K loss increases with shock pressure and starts quite below the conditions of onset of decomposition melting of the micas. However, removal of K from impact melt of terrestrial impact structures has not been reported to date. We think that these observations are not sufficient to determine if K loss may occur or not in the case of a superheated impact melt. Observations that would support this hypothesis include (a) a spatial association of impact melt (or at least melt-bearing suevites) with areas depleted in K and (b) a lower concentration of K in suevite than in the target rock types. Field observations and geological mapping do not suggest any correlation between the occurrence of suevite and the concentration of K, with the caveat that the lack of outcrops in the K-poor moat hinders better understanding of the nature of the underlying material and the real occurrence and spatial distribution of suevite. Analysis of frequency distributions of K in suevite, tektites, and other lithologies does not suggest that melt-bearing material is depleted in K relative to the other lithologies (cf. Fig. 4).

A test to evaluate removal of K from impactites during the impact process could involve isotopic study of K-rich and K-poor areas to examine possible variations of ^{40}K and their correlation with concentrations of K. Signatures of K-loss in impact melt could also be revealed by isotopic analysis of tektites associated with Bosumtwi (Ivory Coast tektites) or other tektite strewn fields with known source craters. The loss of Sn, Cu, and Zn in tektites has been noted from isotopic studies (Creech et al., 2019). However, these elements are moderately volatile elements, unlike K (Creech et al. [2019] and references therein). Taking into account the volatility of these elements, and the relative rates of diffusion in tektite-forming liquid droplets, Humayun and Koeberl (2004) and Creech

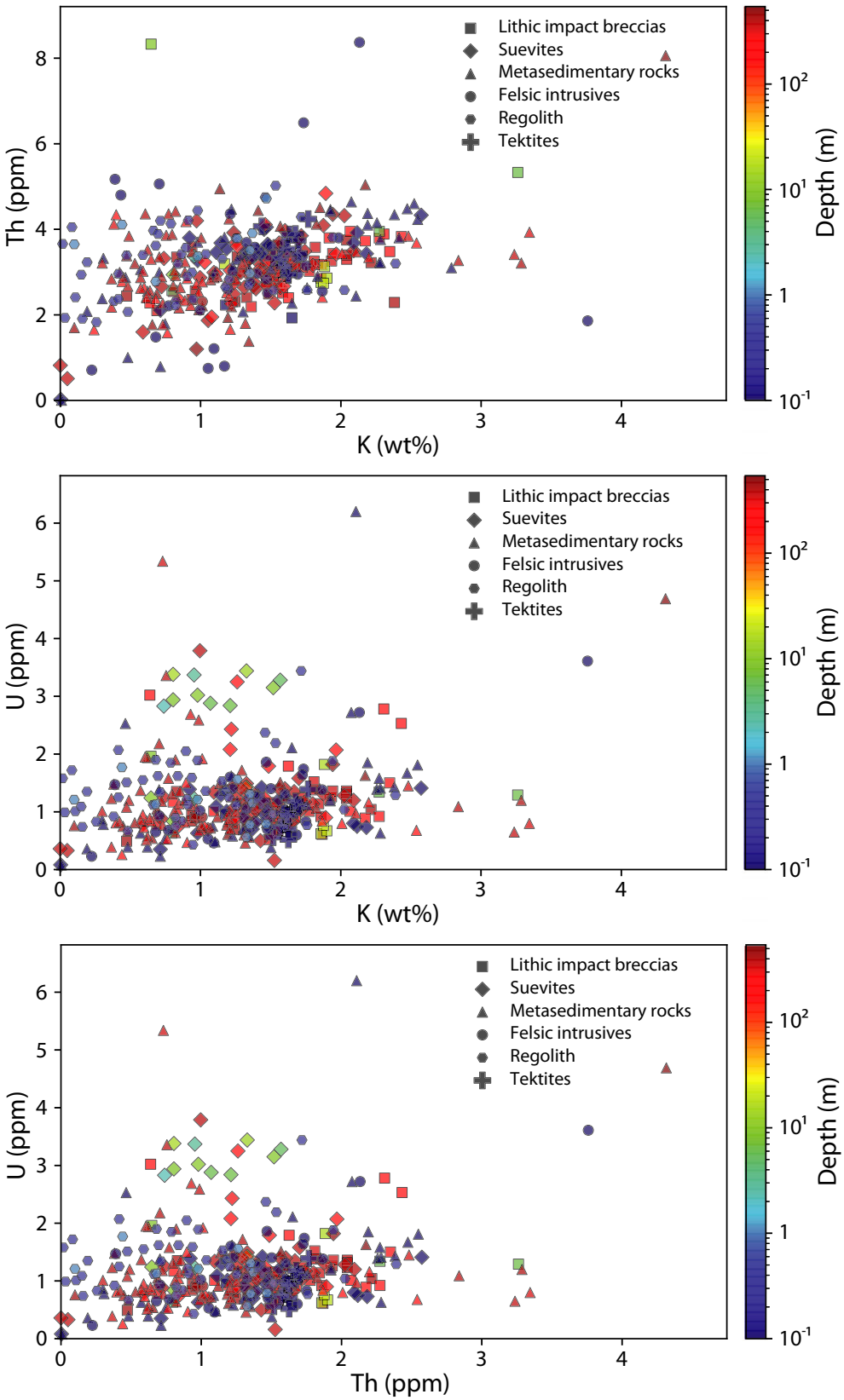

Fig. 10. Potassium, Th, and U concentrations as a function of depth (data from the geochemical database) for the different lithotypes at the Bosumtwi impact structure. (Color figure can be viewed at wileyonlinelibrary.com.)

et al. (2019) concluded that it is unlikely to observe loss of K in impact melts. Considering all the arguments given here, we conclude that the surface patterns of K concentration at Bosumtwi are not likely the result of loss of K as a direct consequence of impact.

Postimpact Redistribution of K By an Impact-Related Hydrothermal System

The passage of the shock wave releases heat that creates a thermal gradient, which, combined with impact-induced fracturing and faulting, and the presence of fluid in the target, may produce a hydrothermal system (Naumov, 2002, 2005; Osinski et al., 2013). Hydrothermal alteration can modify the distribution of mobile elements such as K and U (Bourdon, 2003), leading to an enrichment or depletion in K or U. Potassium metasomatism has been reported, for instance, in the case of the Rochechouart and Shoemaker impact structures (Lambert, 2010; Niang et al., 2021). In these two cases, the impact-related signatures of K and U are restricted to the central area of the impact structure. Hydrothermal activity triggered by impact at Bosumtwi was foreseen by Koeberl and Reimold (2004). Later, Karikari et al. (2007) described two generations of hydrothermal alteration from this impact structure: a preimpact hydrothermal alteration associated with shear zones and characterized by secondary minerals such as chlorite, sericite, sulfides, and quartz, or replacement of some primary minerals, and a later, argillic alteration stage that was found mostly associated with suevite. As suevite locations are restricted to the north and to the south–southwest of the crater rim, no correlation between impact-generated hydrothermal activity and K-rich or K-poor regions can be evaluated.

Postimpact Redistribution of K By Surface Processes

Considering that none of the above hypotheses is able to account for the observed surface variations in K concentration, we have explored the possible role of surface processes and, in particular, erosion and leaching of K during the formation of the lateritic cover and downward advance of the weathering front (Anand & Butt, 2010). A recent survey of the radiometric signature associated with the Australian impact record revealed that postimpact erosion, transport, sedimentation, and weathering are the likely dominant processes responsible for the generation of annular K features associated with impact structures (Niang et al., 2021). In the case of Bosumtwi, a distinct association is noted between the K-rich area of relatively rougher topography and the occurrence of fresh exposures of metasedimentary rock or lithic breccias. In contrast, K-poor areas correspond to the annular moat or occur outside the ejecta deposits, from where saprock and lateritic covers have been reported (Figs. 2 and 8). These observations suggest that the rim and the outer ejecta ridge are currently being eroded, bringing relatively fresh basement rock to surface, whereas in K-poor areas, the K originally present in the metasedimentary rocks has been leached out by fluids. Indeed, we recall here that the development of a lateritic surface in a tropical climate requires a low erosion rate (Beauvais & Chardon, 2013) to facilitate the slow progression of the weathering front with depth (the thickness of the upper layer affected by leaching of mobile elements).

It was possible to directly test these ideas here with cosmogenic nuclide analysis, which confirms low erosion rates within the moat, and higher erosion rates in the rougher areas, such as at the outer ridge. This result can be directly extrapolated to the crater rim. It is, therefore, possible to conclude that the higher erosion rates at the rim and outer ridge are responsible for the annular pattern of exposed K-rich metasedimentary rocks, whereas the comparatively reduced erosion within the moat has enabled the development of a K-poor lateritic surface since the formation of the impact.

Chronological Model of Formation of the K Anomaly

We have thus identified the possible causes for the K-rich double-ring anomaly from the impact process, and we propose that the genesis of this geochemical characteristic results from a redistribution of K by superficial process. Based on field observations, comparison of airborne data and ground-based measurement from FPGRS, and ^{10}Be cosmogenic nuclide studies of surface and boreholes samples, we can infer a plausible scenario to explain the origin of the K anomalies at the Bosumtwi impact structure (Fig. 11). The first step of this model starts at 1 Ma, when a meteoritic projectile hits the surface of the Ashanti belt covered by a thick lateritic (>10 m) cover because of intense weathering under tropical climate. The energy produced by the impact may have exceeded 11,000 MT of TNT equivalent (French, 1998), and a complex crater of 10.5 km in diameter was excavated in the lateritic cover and down to the Birimian metasedimentary strata. Metavolcanic rocks and minor intrusive bodies occurring within the cratered region were also excavated, in part melted, and contributed to the ejecta deposits. Immediately after the impact, the crater topographic expression included a central peak, an uplifted rim, and an ejecta deposit. The presence of volatiles as fluidizing agents (either in the atmosphere or in soil and target rock) led to a ground-hugging flow of

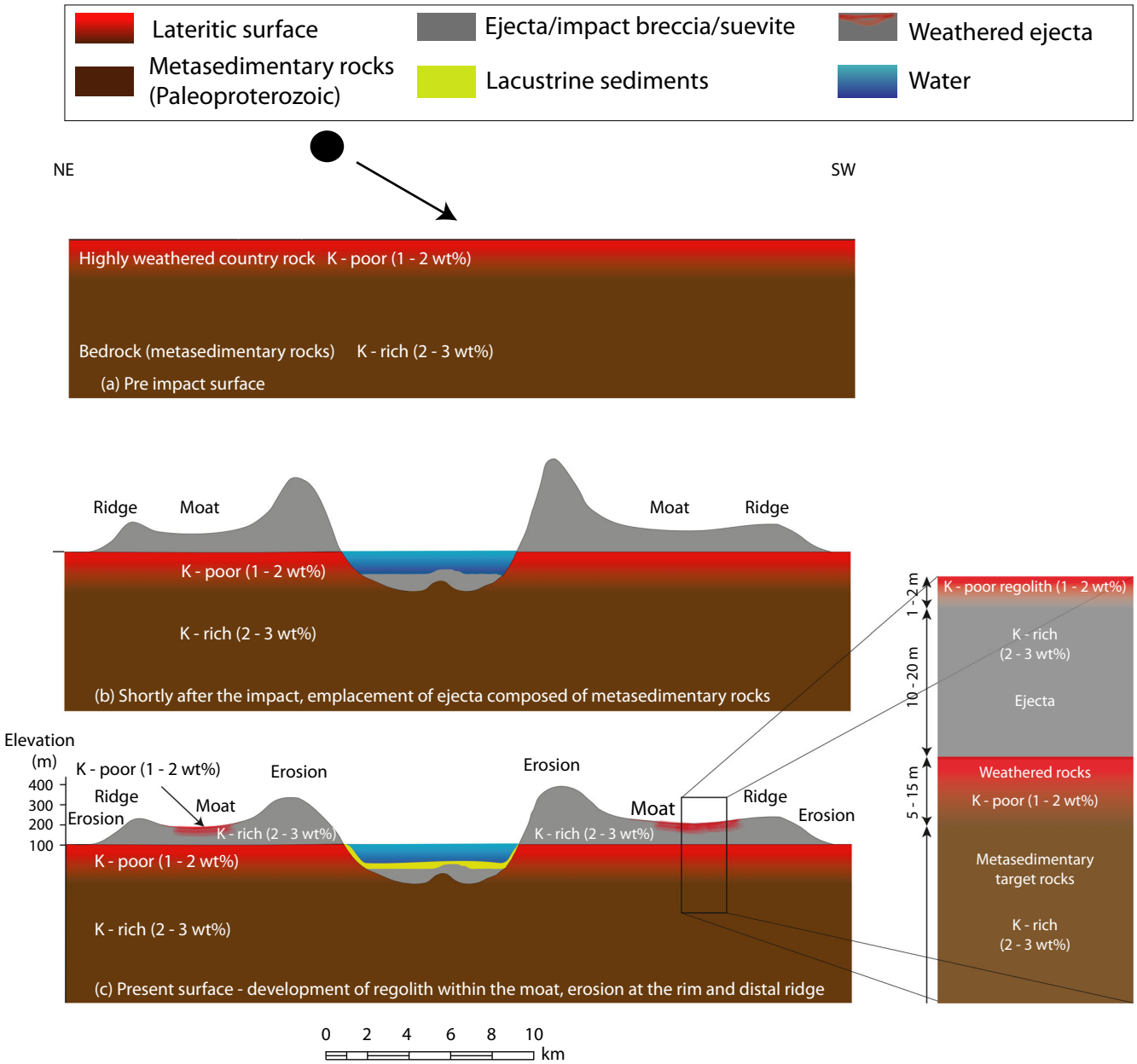

Fig. 11. Left panel: Chronological model for the formation of the K anomaly. a) Preimpact surface. b) Crater shortly after the impact (1 Ma). c) Present time. Right panel: Schematic representation of the variation of the concentration of K within a vertical column through the ejecta at a location in the annular moat. The model is oriented NE-SW, present surface altitude is modified after SRTM (Shuttle Radar Topography Mission) data of 30 m/pixel. (Color figure can be viewed at wileyonlinelibrary.com.)

ejecta leading to the formation of an ejecta morphology including an annular moat and an outer ridge. This ejecta morphology is typical for many impact craters on Mars and has been classified as rampart craters.

Since then, Bosumtwi has been continuously eroded, with strong variations of erosion rates depending on the initial morphology of the impact structure. The crater rim and outer ridge recorded high erosion rates, and comparatively lower erosion rates are assumed elsewhere. The lower erosion rates within the moat favored the development of a new, thin lateritic cover above ejecta deposits. Higher erosion rates at the outer ridge and at the crater rim precluded the formation of such a lateritic cover and left exposures of fresh metasedimentary rock, corresponding to the two annular areas enriched in K.

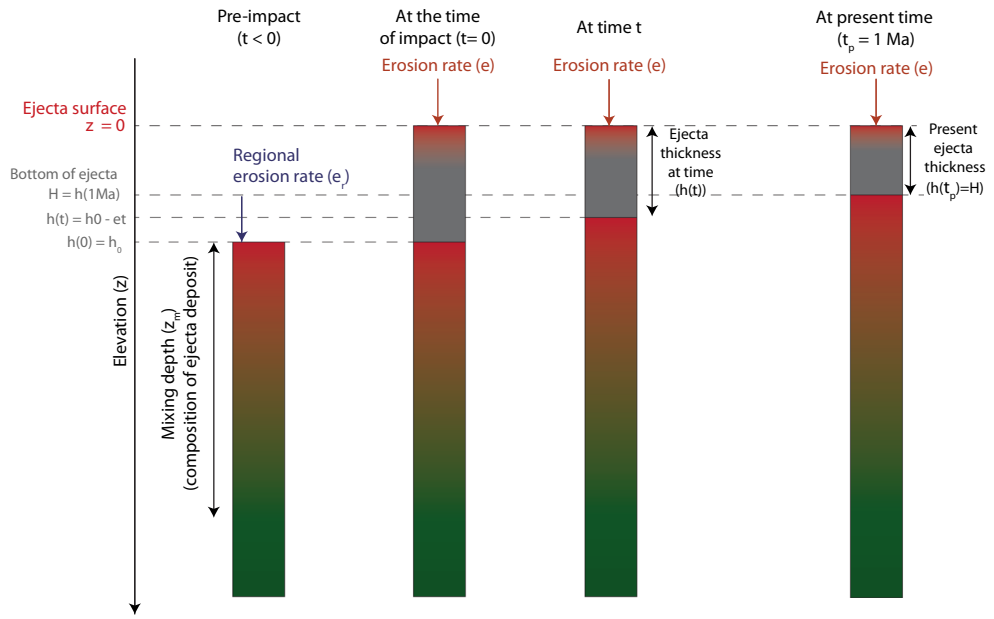

Fig. 12. Model setup for cosmogenic nuclide simulations and parameters. Expected variations (qualitative) of cosmogenic nuclides are represented from green or gray (low) to red (high). (Color figure can be viewed at wileyonlinelibrary.com.)

Cosmogenic Nuclide Simulation and Recommendations For Future Investigations

The value of further cosmogenic nuclide studies can be explored by numerical simulations, which also allows visualization of how our preliminary data are consistent with possible scenarios of ejecta deposition and erosion. Figure 12 presents the model setup, parameters, and expected evolution of cosmogenic nuclide concentrations as a function of time. The reference $z = 0$ corresponds to the ejecta surface, and is, therefore, "moving" as a function of time. The formulation follows Parker and Perg (2005), which reveals the advective nature of modeling the cosmogenic nuclide production in a denuding landscape. The model is designed to predict the expected ^{10}Be concentrations as a function of time, before and after the impact event and as a function of depth, within the ejecta layer and below the ejecta layer.

The equations of nuclide production are given in the Appendix, and the parameters of these equations are given in Table 3. We distinguish the regional (preimpact) erosion rate ε_r (in the absence of the topography generated by the impact) from the local erosion rate (ε). Note that the local erosion rate is assumed to be constant over the ejecta layer, which is certainly not the case, as erosion rates are slope-dependent, whereas large variations of slopes are encountered across the structure from the rim to the outer ejecta ridge. The time reference ($t = 0$) is taken at the time of impact and t_p is the present time; $h(t_p) = H$ represents the present ejecta thickness, $h(t)$ the ejecta thickness at a given time t after impact, and $h(0) = h_0$ the ejecta thickness at the time of impact; z is counted as positive downward. The model equations allow to explore and illustrate the effects of the different parameters (ejecta thickness, regional and postimpact erosion rates) on the present ^{10}Be profiles and also allows a direct comparison of ^{10}Be concentration profiles with ^{10}Be measurements presented in this study.

Figure 13 illustrates the effect of variation of the present ejecta thickness from 10 to 30 m with fixed regional and postimpact erosion rates (respectively, 2.5 m 10^6 yr^{-1} and 5 m/10^6 yr^{-1}). Note that the present ejecta thickness is a priori known from core logging.

In BH1, the reported ejecta thickness is >15 m, and in BH3, it is 10 m. These simulations illustrate how the results are sensitive to this parameter, which is considered well constrained by previous work on the drill cores (Boamah & Koeberl, 2003). In Fig. 14, the preimpact erosion rate is fixed (2.5 m 10^6 yr^{-1}) and the concentrations of ^{10}Be at depth are calculated for two different values of postimpact erosion rates of 5.0 m 10^6 yr^{-1} and 0.1 m 10^6 yr^{-1}. The present ejecta thicknesses are fixed based on core observations (15 m for BH1, and 10 m for BH3). In Fig. 15, the effect of varying the regional erosion rate (preimpact) is illustrated with values of 2.5 m 10^6 yr^{-1} and 50 m 10^6 yr^{-1}. Measured ^{10}Be concentrations are added to the simulation plots: ^{10}Be concentrations of core samples are presented in blue and ^{10}Be measurements in rock samples collected at the near surface are represented in red.

Table 3. List of parameters related to cosmogenic nuclide decay and production (Dunai, 2010).

Definition	Symbol	Value	Value (S.I.)
Rock density (metasedimentary)	ρ	2.5 g cm^{-3}	2500 kg m^{-3}
Half-life	$t_{1/2}$	1,387,000 yr	4.378*10^{12} s
Decay rate	λ	4.997*10^{-7} yr^{-1}	1.584*10^{-14} s^{-1}
Surface production (neutrons)	P_{0n}	2.89 at g^{-1} a^{-1}	9.1579*10^{-5} at kg^{-1} s^{-1}
Surface production (slow muons)	P_{0s}	0.0132 at g^{-1} a^{-1}	4.1828*10^{-7} at kg^{-1} s^{-1}
Surface production (fast muons)	P_{0f}	0.0421 at g^{-1} a^{-1}	1.3341*10^{-6} at kg^{-1} s^{-1}
Attenuation length neutrons	Λ_n	160 g cm^{-2}	1600 kg m^{-2}
Attenuation length slow muons	Λ_s	1500 g cm^{-2}	15,000 kg m^{-2}
Attenuation fast muons	Λ_f	4320 g cm^{-2}	43,200 kg m^{-2}
Attenuation factor neutrons	$\nu_n = \rho/\Lambda_n$	1.5625*10^{-2} cm^{-1}	1.5625 m^{-1}
Attenuation factor slow muons	$\nu_s = \rho/\Lambda_s$	1.667*10^{-3} cm^{-1}	0.1667 m^{-1}
Attenuation factor fast muons	$\nu_f = \rho/\Lambda_f$	5.78*10^{-4} cm^{-1}	0.0578 m^{-1}

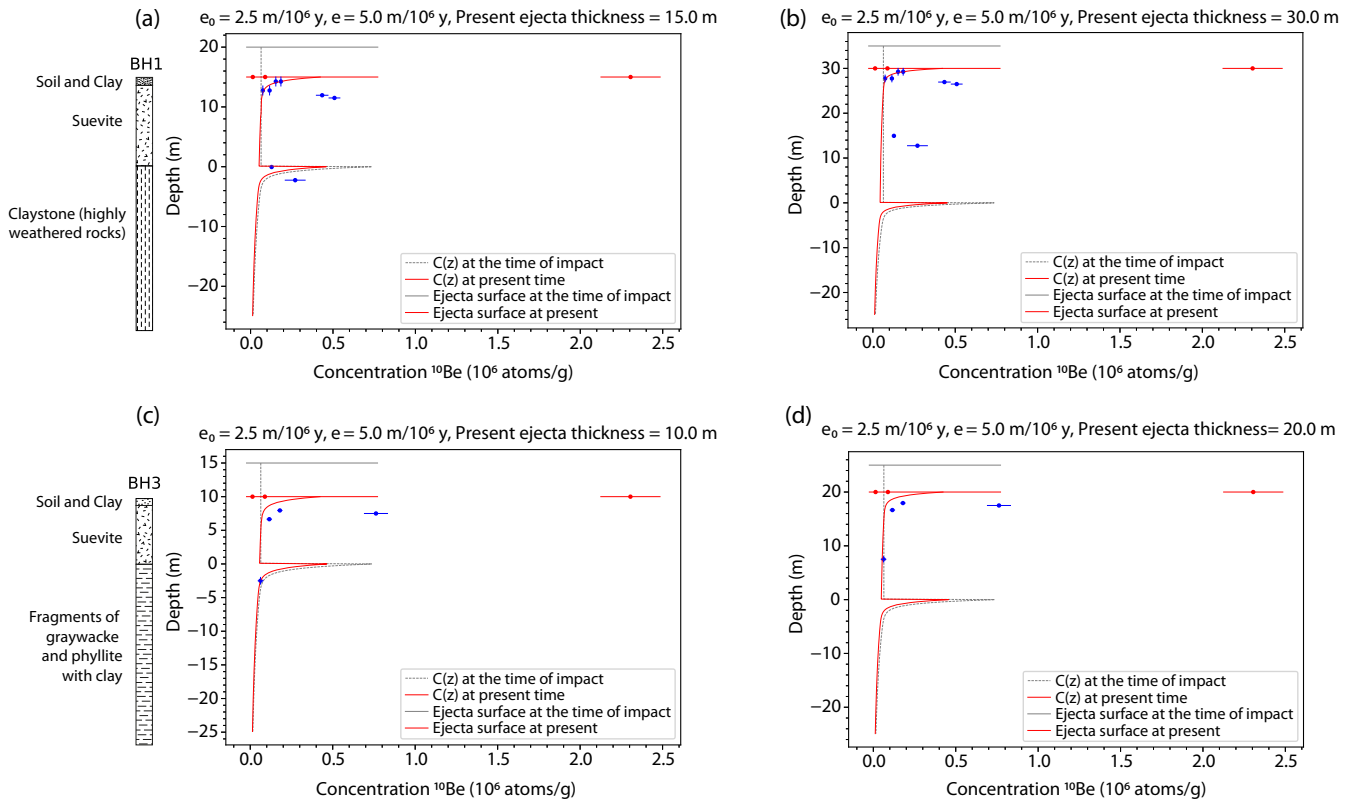

Fig. 13. Numerical models of ^{10}Be concentrations as function of erosion rates and ejecta thicknesses in BH1 and BH3. Preimpact and postimpact erosion rates are fixed at 2.5 m 10^6 yr^{-1} and 5.0 m 10^6 yr^{-1}, respectively. a) BH1 with 15 m ejecta thickness, b) BH1 with 30 m ejecta thickness. c) BH3 with 10 m ejecta thickness. d) BH3 with 20 m ejecta thickness. Red circles indicate surface data and blue circles indicate subsurface data. (Color figure can be viewed at wileyonlinelibrary.com.)

This initial test shown in Fig. 13 with variation of ejecta thicknesses was done to check if the ^{10}Be concentrations are, to the first order, consistent with emplacement of 15 m of ejecta at 1 Myr ago over a lateritic surface that was previously exposed to cosmic rays (cosmogenic nuclide production before it was buried at 1 Myr ago). The ^{10}Be concentrations in samples of BH1 are indeed more consistent with an ejecta thickness of 15 m, rather than with a 30 m ejecta thickness. The same inference could not be drawn based on BH3 samples, as the low ^{10}Be concentration of the lower sample is, within error bars, consistent with both values of ejecta thickness (Figs. 13c and 13d). As shown in Fig. 14, none of the simulations can produce a perfect match with observed ^{10}Be concentrations, and a more complex history than the scenario presented in the Chronological Model of Formation of the K Anomaly section must be considered to account for all the data. The

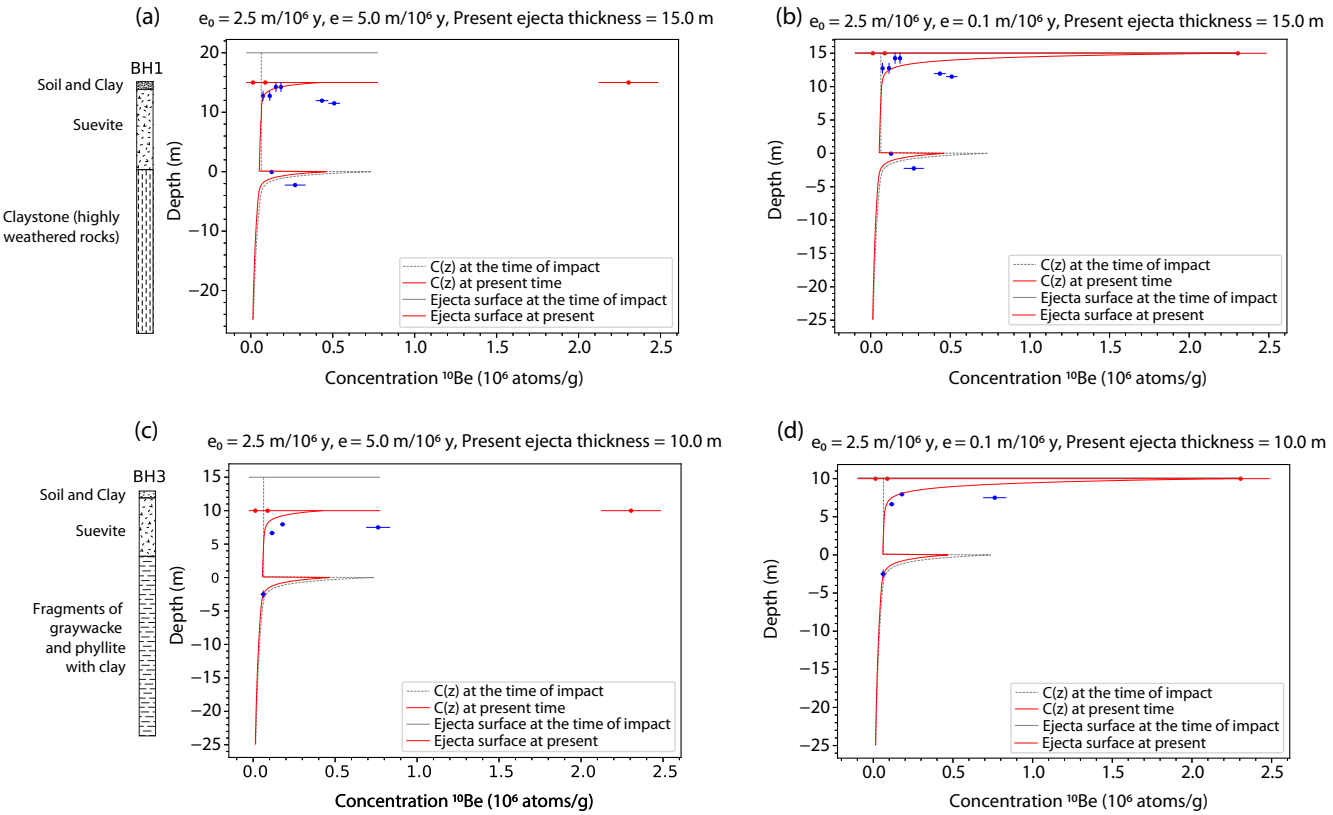

Fig. 14. Numerical models of ^{10}Be concentrations as function of erosion rates and ejecta thicknesses in BH1 and BH3. Preimpact erosion rate is fixed at 2.5 m/10^6 yr. a) BH1, postimpact erosion rate of 5.0 m 10^6 yr^{-1}, and 15 m ejecta thickness. b) BH1, postimpact erosion rate of 0.1 m 10^6 yr^{-1}, and 15 m ejecta thickness. c) BH3, postimpact erosion rate of 5.0 m 10^6 yr^{-1}, and 10 m ejecta thickness. d) BH3, postimpact erosion rates of 0.1 m 10^6 yr^{-1}, and 10 m ejecta thickness. Red circles indicate surface data and blue circles indicate subsurface data. (Color figure can be viewed at wileyonlinelibrary.com.)

rise of ^{10}Be concentrations in the ejecta layer around 3–3.5 m depth could, for instance, reflect localized mass movement. Samples exposed at the surface, then buried during the impact event, could explain the nonmonotonous variations of ^{10}Be at depth. Alternatively, these variations may be inherited from mixing during ejecta emplacement, as previously observed in the impact breccia (Losiak et al., 2014), with the partial preservation of reservoirs of variable ^{10}Be concentrations, originating from surface or subsurface environments. Another process to consider in interpreting near-surface concentrations is bioturbation. Bioturbation is common in tropical areas and results in mixing of superficial material with deeper material (typically, down to 1–2 m depth). With respect to the exponential profile, bioturbation could increase the concentrations of cosmogenic nuclides at depth and decrease the concentrations observed at surface. However, including bioturbation and erosion would not suffice to explain the nonmonotonic variations of cosmogenic nuclide concentrations in BH1 and surface samples. The elevated concentration of ^{10}Be in one of the surface samples suggests that, locally, erosion rates as low as 0.1 m Ma^{-1} are possible in the moat. Last, a regional erosion rate as high as 50 m Myr^{-1} clearly does not match our observations. This confirms that the regional erosion rates are low in the absence of significant topography/slopes (exceptions being the crater rim and outer ridge). Finally, the comparison between BH1 and BH3, which were drilled only a few hundred meters apart, reveals that a large gradient of erosion rates is possible within the impact structure: the surface at BH1 would have been more rapidly eroded than that at BH3. Such variations are consistent with the present location of BH1, closer to the crater rim, and BH3, closer to the central part of the moat (Fig. 16).

These simulations provide a framework to define a future field campaign dedicated to cosmogenic nuclide studies. Samples should be taken at variable depths (between 0 and 3 meters) at the crater rim and at the outer ridge to confirm the comparatively higher erosion rates at these locations. We also recommend to conduct further analyses on the BH1/BH3 cores across the contact between ejecta and preimpact surface. Such data should provide new information about mixing during

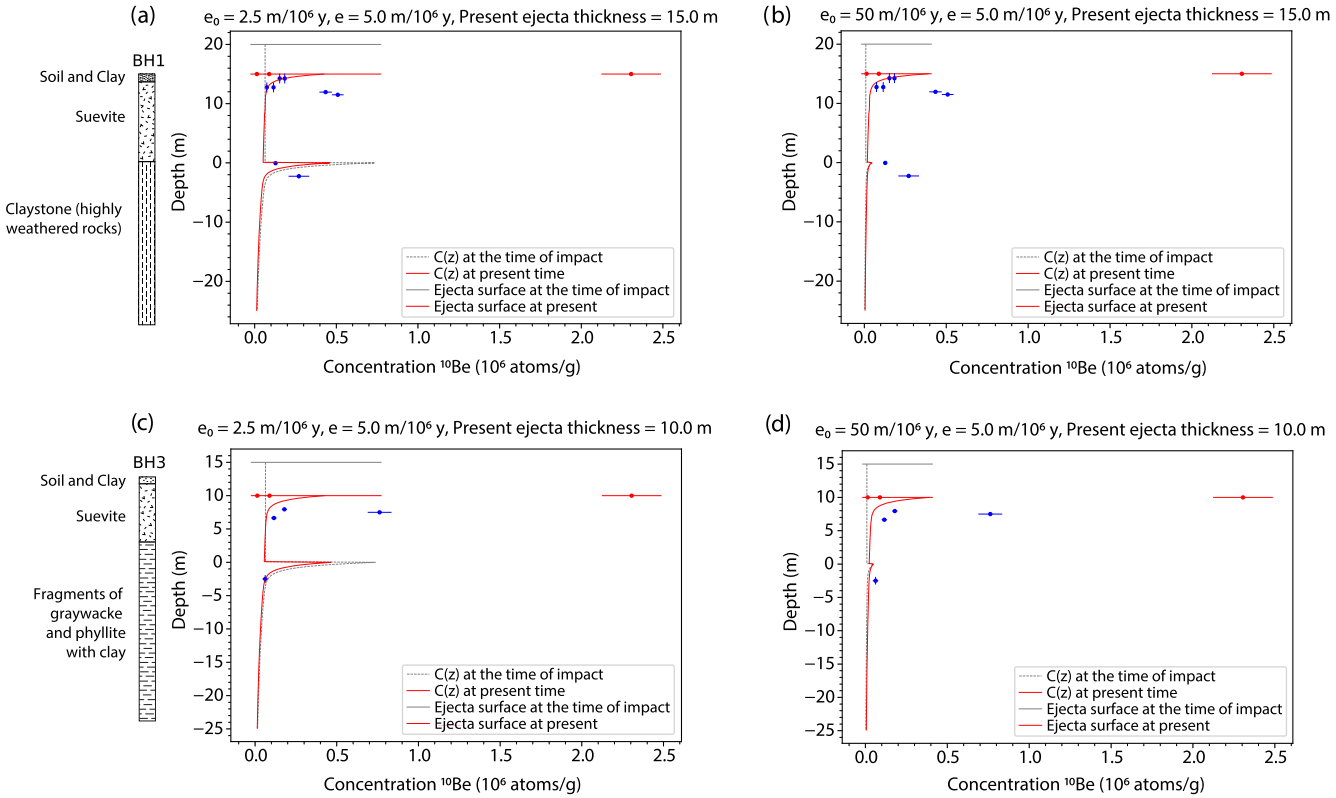

Fig. 15. Numerical models of ^{10}Be concentrations as function of erosion rates and ejecta thicknesses in BH1 and BH3. Postimpact erosion rate is fixed at 5.0 m 10^6 yr^{-1}. Ejecta thickness is 15 m for BH1, 10 m for BH3, based on core data. a) Preimpact erosion rate of 2.5 m 10^6 yr^{-1}. b) Preimpact erosion rates of 50.0 m 10^6 yr^{-1}. c) Preimpact erosion rate of 2.5 m 10^6 yr^{-1}. d) Preimpact erosion rates of 50.0 m 10^6 yr^{-1}. Red circles indicate surface data and blue circles indicate subsurface data. (Color figure can be viewed at wileyonlinelibrary.com.)

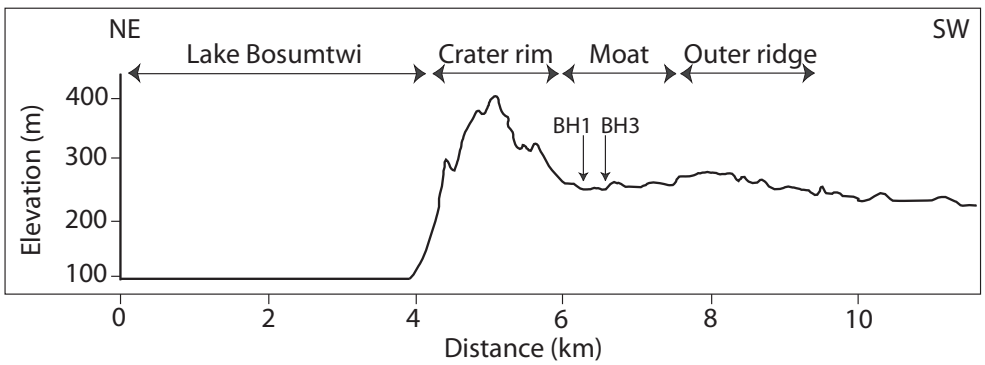

Fig. 16. Radial profile from lake center outwards from the Bosumtwi impact structure (see Fig. 4 for ground track) with the location of BH1 and BH3 (moat). Data source: SRTM of 30 m/pixel resolution.

ejecta emplacement, which is particularly relevant when considering the analogy that has been made between the ejecta of Bosumtwi and the fluidized (water-rich) emplacement of ejecta of rampart craters on Mars (Baratoux, Niang, et al., 2019; Wulf et al., 2019).

CONCLUSIONS

The nature of the K-poor (regolith) and K-rich material (metasedimentary rocks and lithic impact breccias) forming an annular pattern in the airborne

radiometric survey of the Bosumtwi impact structure is determined from field observations and in situ FPGRS measurements. Our study reveals that the annular feature of elevated K concentrations is not related to mobilization of K as a direct consequence of the impact. Variations of K concentrations as a function of basement lithology reflected in ejecta emplacement do not appear to control the annular pattern of K concentrations either. Based on the field observations and K, Th, and U ground-based measurements on rocks and soils throughout the impact structure in both K-poor and K-rich areas, we conclude that the annular potassium anomaly is due to a competition between spatially variable erosion rates within the impact structure and the development of a new lateritic surface since the formation of the crater. Our ^{10}Be analyses seem to confirm low erosion rates in the moat between crater rim and external ridge, as well as seemingly large variations of erosion rates across the structure. Additional beryllium isotopic analyses are required to further investigate this. The present study highlights the value of airborne radiometric surveys in impact science, and as a source of information about surface processes. Impact structures are seemingly commonly associated with radiometric anomaly signatures (Niang et al., 2021; Pesonen et al., 2003; Vasconcelos et al., 2012), and these appear to be often related to postimpact processes rather than directly impact-related or impact-induced hydrothermal processes. Even if the radiometric signatures are indirectly related to the impact, the formation of nearly circular patterns in K, Th, and U maps may provide a complementary tool for the recognition of potential impact structures.

Acknowledgments—This research has been achieved in the framework of the research and higher education network "African Initiative for Planetary and Space Science." C.A.B. Niang received a grant from the Barringer Family Fund for Meteorite Impact Research and a Ph.D. fellowship of the French Embassy in Senegal for his visit in France. This research also received the support of the INSU/CNRS and the French National Research Institute for Sustainable Development. C.A.B. Niang also received financial support from the Center for International Research & Restitution on Impacts and on Rochechouart (CIRIR) as a contribution to his PhD thesis. W.U.R. acknowledges research support from the Brazilian CNPq, and his studies since 2018 have been financed in part by the Coordenação de Aperfeiçoamento de Pessoal de Nivel Superior—Brasil (CAPES)—Finance Code 001 (project 309878/2019-5). The authors thank reviewer G. Balco and an anonymous reviewer, the associate editor Marc Caffee, and the editor-in-chief A.J. Timothy Jull for their editorial handling of the manuscript.

Data Availability Statement—Data openly available in a public repository that issues datasets with DOIs.

Editorial Handling—Dr. Marc Caffee

REFERENCES

Anand, R. R., and Butt, C. R. M. 2010. A Guide for Mineral Exploration Through the Regolith in the Yilgarn Craton, Western Australia. *Australian Journal of Earth Sciences* 57: 1015–114.

Baloga, S. M. 2005. Emplacement of Martian Rampart Crater Deposits. *Journal of Geophysical Research* 110: E10001. https://doi.org/10.1029/2004JE002338.

Baratoux, D., Baratoux, L., Olivier, P., McFarlane, H., Ahrin, E., Jessell, M.W., Block, S. et al. 2014. First Tests and Results in the Wa-lawra, Bole-nangodi, Sefwi and Bui Belts, Ghana (Abstract). 25th Colloquium of African Geology, Dar Es Salaam, Tanzania.

Baratoux, D., Niang, C. A. B., Reimold, W. U., Sapah, M. S., Jessell, M. W., Boamah, D., Faye, G., Bouley, S., and Vanderhaeghe, O. 2019. Bosumtwi Impact Structure, Ghana: Evidence for Fluidized Emplacement of the Ejecta. *Meteoritics & Planetary Science* 54: 2541–56. https://doi.org/10.1111/maps.13253.

Baratoux, D., Pinet, P., Gendrin, A., Kanner, L., Mustard, J., Daydou, Y., Vaucher, J., and Bibring, J.-P. 2007. Mineralogical Structure of the Subsurface of Syrtis Major from Omega Observations of Lobate Ejecta Blankets: Mineralogy of Ejecta at Syrtis Major. *Journal of Geophysical Research: Planets* 112. https://doi.org/10.1029/2007JE002890.

Baratoux, L., Söderlund, U., Ernst, R. E., De Roever, E., Jessell, M. W., Kamo, S., Naba, S. et al. 2019. New U-Pb Baddeleyite Ages of Mafic Dyke Swarms of the West African and Amazonian Cratons: Implication for Their Configuration in Supercontinents Through Time. In *Dyke Swarms of the World: A Modern Perspective*, edited by R. K. Srivastava, R. E. Ernst, and P. Peng, 263–314. Singapore: Springer Singapore.

Barlow, N. G., Boyce, J. M., Costard, F. M., Craddock, R. A., Garvin, J. B., Sakimoto, S. E. H., Kuzmin, R. O., Roddy, D. J., and Soderblom, L. A. 2000. Standardizing the Nomenclature of Martian Impact Crater Ejecta Morphologies. *Journal of Geophysical Research: Planets* 105: 26,733–8. https://doi.org/10.1029/2002JE002036.

Beauvais, A., and Chardon, D. 2013. Modes, Tempo, and Spatial Variability of Cenozoic Cratonic Denudation: The West African Example: Cenozoic Cratonic Denudation. *Geochemistry, Geophysics, Geosystems* 14: 1590–608. https://doi.org/10.1002/ggge.20093.

Boamah, D., and Koeberl, C. 2002. Geochemistry of Soils from the Bosumtwi Impact Structure, Ghana, and Relationship to Radiometric Airborne Geophysical Data. In *Meteoritic Impacts in Precambrian Shields*, edited by J.

Plado and L. J. Pesonen, 211–55. Impact Studies, volume 2. Berlin: Springer.

Boamah, D., and Koeberl, C. 2003. Geology and Geochemistry of Shallow Drill Cores from the Bosumtwi Impact Structure, Ghana. *Meteoritics & Planetary Science* 38: 1137–59. https://doi.org/10.1111/j.1945-5100.2003.tb00304.x.

Boamah, D., and Koeberl, C. 2006. Petrographic Studies of "Fallout" Suevite from Outside the Bosumtwi Impact Structure, Ghana. *Meteoritics & Planetary Science* 41: 1761–74. https://doi.org/10.1111/j.1945-5100.2006.tb00450.x.

Bourdon, B. 2003. Introduction to U-Series Geochemistry. *Reviews in Mineralogy and Geochemistry* 52: 1–21. https://doi.org/10.2113/0520001.

Braucher, R., Guillou, V., Bourlès, D. L., Arnold, M., Aumaître, G., Keddadouche, K., and Nottoli, E. 2015. Preparation of ASTER In-House $^{10}Be/^{9}Be$ Standard Solutions. *Nuclear Instruments and Methods in Physics Research Section B: Beam Interactions with Materials and Atoms* 361: 335–40.

Brown, E. T., Stallard, R. F., Larsen, M. C., Raisbeck, G. M., and Yiou, F. 1995. Denudation Rates Determined from the Accumulation of In Situ-Produced 10Be in the Luquillo Experimental Forest, Puerto Rico. *Earth and Planetary Science Letters* 129: 193–202. https://doi.org/10.1016/0012-821X(94)00249-X.

Chmeleff, J., von Blanckenburg, F., Kossert, K., and Jakob, D. 2010. Determination of the ^{10}Be Half-Life by Multicollector ICP-MS and Liquid Scintillation Counting. *Nuclear Instruments and Methods in Physics Research Section B: Beam Interactions with Materials and Atoms* 268: 192–9. https://doi.org/10.1016/j.nimb.2009.09.012.

Coney, L., Gibson, R. L., Reimold, W. U., and Koeberl, C. 2007. Lithostratigraphic and Petrographic Analysis of ICDP Drill Core LB-07A, Bosumtwi Impact Structure, Ghana. *Meteoritics & Planetary Science* 42: 569–89. https://doi.org/10.1111/j.1945-5100.2007.tb01062.x.

Creech, J. B., Moynier, F., and Koeberl, C. 2019. Volatile Loss Under a Diffusion-Limited Regime in Tektites: Evidence from Tin Stable Isotopes. *Chemical Geology* 528: 119279. https://doi.org/10.1016/j.chemgeo.2019.119279.

Dai, X., Boamah, D., Koeberl, C., Reimold, W. U., Irvine, G., and McDonald, I. 2005. Bosumtwi Impact Structure, Ghana: Geochemistry of Impactites and Target Rocks, and Search for a Meteoritic Component. *Meteoritics & Planetary Science* 40: 1493–511. https://doi.org/10.1111/j.1945-5100.2005.tb00414.x.

Dunai, T. J. 2010. *Cosmogenic Nuclides: Principles, Concepts and Applications in the Earth Surface Sciences*. Cambridge, UK: Cambridge University Press.

Fall, M., Baratoux, D., Jessell, M., Ndiaye, P. M., Vanderhaeghe, O., Moyen, J. F., Baratoux, L., and Bonzi, W.-M.-E. 2020. The Redistribution of Thorium, Uranium, Potassium by Magmatic and Hydrothermal Processes Versus Surface Processes in the Saraya Batholith (Eastern Senegal): Insights from Airborne Radiometrics Data and Topographic Roughness. *Journal of Geochemical Exploration* 219: 106633. https://doi.org/10.1016/j.gexplo.2020.106633.

Fall, M., Baratoux, D., Ndiaye, P. M., Jessell, M., and Baratoux, L. 2018. Multi-Scale Distribution of Potassium. Thorium and Uranium in Paleoproterozoic Granites from Eastern Senegal. *Journal of African Earth Sciences* 148: 30–51. https://doi.org/10.1016/j.jafrearsci.2018.03.026.

Ferrière, L., Koeberl, C., Brandstätter, F., and Mader, D. 2010. Geochemistry of Basement Rocks and Impact Breccias from the Central Uplift of the Bosumtwi Crater, Ghana—Comparison of Proximal and Distal Impactites. In *Large Meteorite Impacts and Planetary Evolution IV*, edited by W. U. Reimold and R. L. Gibson. Geological Society of America 465: 645–51.

Ferriere, L., Koeberl, C., Ivanov, B. A., and Reimold, W. U. 2008. Shock Metamorphism of Bosumtwi Impact Crater Rocks, Shock Attenuation, and Uplift Formation. *Science* 322: 1678–81. https://doi.org/10.1126/science.1166283.

Ferrière, L., Koeberl, C., and Reimold, W. U. 2007. Drill Core LB-08A, Bosumtwi Impact Structure, Ghana: Petrographic and Shock Metamorphic Studies of Material from the Central Uplift. *Meteoritics & Planetary Science* 42: 611–33.

French, B. M. 1998. *Traces of Catastrophe: A Handbook of Shock-Metamorphic Effects in Terrestrial Meteorite Impact Structures*. Houston, TX: Lunar and Planetary Science Institute.

Goldfarb, R. J., André-Mayer, A.-S., Jowitt, S. M., and Mudd, G. M. 2017. West Africa: The World's Premier Paleoproterozoic Gold Province. *Economic Geology* 112: 123–43. https://doi.org/10.2113/econgeo.112.1.123.

Gottwald, M., Kenkmann, T., and Reimold, W. U. 2020. *Terrestrial Impact Structures: The TanDEM-X Atlas. Part 1 and 2*, 605. Munich: Dr.-Friedrich-Pfeil Verlag.

Granger, D. E., Kirchner, J. W., and Finkel, R. 1996. Spatially Averaged Long-Term Erosion Rates Measured from in Situ-Produced Cosmogenic Nuclides in Alluvial Sediment. *The Journal of Geology* 104: 249–57. https://doi.org/10.1086/629823.

Humayun, M., and Clayton, R. N. 1995. Precise Determination of the Isotopic Composition of Potassium: Application to Terrestrial Rocks and Lunar Soils. *Geochimica et Cosmochimica Acta* 59: 2115–30. https://doi.org/10.1016/0016-7037(95)00131-X.

Humayun, M., and Koeberl, C. 2004. Potassium Isotopic Composition of Australasian Tektites. *Meteoritics & Planetary Science* 39: 1509–16. https://doi.org/10.1111/j.1945-5100.2004.tb00125.x.

Jiang, Y., Chen, H., Fegley, B., Lodders, K., Hsu, W., Jacobsen, S. B., and Wang, K. 2019. Implications of K, Cu and Zn Isotopes for the Formation of Tektites. *Geochimica et Cosmochimica Acta* 259: 170–87.

Jones, W. B. 1985. Chemical Analyses of Bosumtwi Crater Target Rocks Compared with the Ivory Coast Tektites. *Geochimica et Cosmochimica Acta* 49: 2569–76. https://doi.org/10.1016/0016-7037(85)90126-7.

Jones, W. B., Bacon, M., and Hastings, D. A. 1981. The Lake Bosumtwi Impact Crater, Ghana. *Geological Society of America Bulletin* 92: 342–9.

Junner, N. R. 1937. The Geology of the Bosumtwi Caldera and Surrounding Country: Gold Coast. *Geological Survey Bulletin* 8: 1–38.

Karikari, F., Ferrière, L., Koeberl, C., Reimold, W. U., and Mader, D. 2007. Petrography, Geochemistry, and Alteration of Country Rocks from the Bosumtwi Impact Structure, Ghana. *Meteoritics & Planetary Science* 42: 513–40. https://doi.org/10.1111/j.1945-5100.2007.tb01058.x.

Koeberl, C., Bottomley, R., Glass, B. P., and Storzer, D. 1997. Geochemistry and Age of Ivory Coast Tektites and Microtektites. *Geochimica et Cosmochimica Acta* 61: 1745–72. https://doi.org/10.1016/S0016-7037(97)00026-4.

Koeberl, C., Milkereit, B., Overpeck, J. T., Scholz, C. A., Amoako, P. Y. O., Boamah, D., Danuor, S. K. et al. 2007. An International and Multidisciplinary Drilling Project into a Young Complex Impact Structure: The 2004 ICDP Bosumtwi Crater Drilling Project—An Overview. *Meteoritics & Planetary*

Science 42: 483–511. https://doi.org/10.1111/j.1945-5100.2007.tb01057.x.

Koeberl, C., and Reimold, W. U. 2005. Bosumtwi Impact Crater, Ghana (West Africa): An Updated and Revised Geological Map, with Explanations. *Jahrbuch der Geologischen Bundesanstalt, Wien (Yearbook of the Austrian Geological Survey)* 145: 31–70 (+ 1 map, 1:50,0000).

Koeberl, C., and Reimold, W. U. 2004 Post-Impact Hydrothermal Activity in Meteorite Impact Craters and Potential Opportunities for Life. In *Bioastronomy 2002: Life Among the Stars*, edited by R. Norris, and F. Stootman, 299. San Francisco, CA: Astronomical Society of the Pacific.

Koeberl, C., Reimold, W. U., Blum, J. D., and Chamberlain, C. P. 1998. Petrology and Geochemistry of Target Rocks from the Bosumtwi Impact Structure, Ghana, and Comparison with Ivory Coast Tektites. *Geochimica et Cosmochimica Acta* 62: 2179–96.

Kolbe, P., Pinson, W. H., Saul, J. M., and Miller, E. W. 1967. Rb-Sr Study on Country Rocks of the Bosumtwi Crater, Ghana. *Geochimica et Cosmochimica Acta* 31: 869–75. https://doi.org/10.1016/S0016-7037(67)80035-8.

Korschinek, G., Bergmaier, A., Faestermann, T., Gerstmann, U. C., Knie, K., Rugel, G., Wallner, A. et al. 2010. A New Value for the Half-Life of ^{10}Be by Heavy-Ion Elastic Recoil Detection and Liquid Scintillation Counting. *Nuclear Instruments and Methods in Physics Research Section B: Beam Interactions with Materials and Atoms* 268: 187–91. https://doi.org/10.1016/j.nimb.2009.09.020.

Lambert, P. 2010. Target and Impact Deposits at Rochechouart Impact Structure, France. In: *Large Meteorite Impacts and Planetary Evolution IV*, edited by R. L. Gibson and W. U. Reimold. GSA Special Paper 465: 509–41. https://doi.org/10.1130/2010.2465(25).

Lambert, P., and MacKinnon, I. D. R. 1984. Micas in Experimentally Shocked Gneiss. *Journal of Geophysical Research* 89: B685–99. https://doi.org/10.1029/JB089iS02p0B685.

Leube, A., Hirdes, W., Mauer, R., and Kesse, G. O. 1990. The Early Proterozoic Birimian Supergroup of Ghana and Some Aspects of its Associated Gold Mineralization. *Precambrian Research* 46: 139–65. https://doi.org/10.1016/0301-9268(90)90070-7.

Lodders, K. 2003. Solar System Abundances and Condensation Temperatures of the Elements. *The Astrophysical Journal* 591: 1220–47.

Losiak, A., Schulz, T., Buchwaldt, R., and Koeberl, C. 2013. Petrology, Major and Trace Element Geochemistry, Geochronology, and Isotopic Composition of Granitic Intrusions from the Vicinity of the Bosumtwi Impact Crater, Ghana. *Lithos* 177: 297–313. https://doi.org/10.1016/j.lithos.2013.06.002.

Losiak, A., Wild, E. M., Michlmayr, L., and Koeberl, C. 2014. ^{10}Be Content in Clasts from Fallout Suevitic Breccia in Drill Cores from the Bosumtwi Impact Crater, Ghana: Clues to Preimpact Target Distribution. *Meteoritics & Planetary Science* 49: 394–411. https://doi.org/10.1111/maps.12256.

McDonald, I., Peucker-Ehrenbrink, B., Coney, L., Ferrière, L., Reimold, W. U., and Koeberl, C. 2007. Search for a Meteoritic Component in Drill Cores from the Bosumtwi Impact Structure, Ghana: Platinum Group Element Contents and Osmium Isotopic Characteristics. *Meteoritics & Planetary Science* 42: 743–53. https://doi.org/10.1111/j.1945-5100.2007.tb01071.x.

Milési, J. P., Feybesse, J. L., Pinna, P., Deschamps, Y., Kampunzu, H., Muhongo, S., Lescuyer, J. L. et al. 2004. Geological Map of Africa 1:10 000 000, SIGAfrique Project. In: *20th Conference of African Geology*. Orleáns, France: BRGM.

Moon, P. A., and Mason, D. 1967. The Geology of 1⁄4 Field Sheets 129 and 131, Bompata S. W. and N. W. *Ghana Geological Survey Bulletin* 31: 1–51.

Naumov, M. V. 2002. Impact-Generated Hydrothermal Systems: Data from Popigai, Kara, and Puchezh-Katunki Impact Structures. In *Impacts in Precambrian Shields*, edited by J. Plado and L. J. Pesonen, 117–71. Berlin: Springer.

Naumov, M. V. 2005. Principal Features of Impact-Generated Hydrothermal Circulation Systems: Mineralogical and Geochemical Evidence. *Geofluids* 5: 165–84. https://doi.org/10.1111/j.1468-8123.2005.00092.x.

Niang, C. A. B., Baratoux, D., Diallo, D. P., Rochette, P., Jessell, M. W., Reimold, W. U., Bouley, S., Vanderhaeghe, O., Faye, G., and Lambert, P. 2021. Systematic Survey of K, Th, and U Signatures in Airborne Radiometric Data from Australian Meteorite Impact Structures: Possible Causes of Circular Features and Implications. In *Large Meteorite Impacts and Planetary Evolution VI*, edited by W. U. Reimold and C. Koeberl. Geological Society of America Special Paper 550: 373–405. https://doi.org/10.1130/2021.2550(15).

Nishiizumi, K. 2004. Preparation of ^{26}Al AMS Standards. *Nuclear Instruments and Methods in Physics Research Section B: Beam Interactions with Materials and Atoms* 223–224: 388–92. https://doi.org/10.1016/j.nimb.2004.04.075.

Osinski, G. R., Tornabene, L. L., Banerjee, N. R., Cockell, C. S., Flemming, R., Izawa, M. R. M., McCutcheon, J. et al. 2013. Impact-Generated Hydrothermal Systems on Earth and Mars. *Icarus* 224: 347–63. https://doi.org/10.1016/j.icarus.2012.08.030.

Parker, G., and Perg, L. A. 2005. Probabilistic Formulation of Conservation of Cosmogenic Nuclides: Effect of Surface Elevation Fluctuations on Approach to Steady State. *Earth Surface Processes and Landforms* 30: 1127–44. https://doi.org/10.1002/esp.1266.

Pesonen, L. J., Koeberl, C., and Hautaniemi, H. 2003. Airborne Geophysical Survey of the Lake Bosumtwi Meteorite Impact Structure (Southern Ghana): Geophysical Maps with Descriptions. *Jahrbuch der Geologischen Bundesanstalt, Vienna, Yearbook of the Australian Geological Survey* 143: 581–604.

Ramsey, M. S. 2002. Ejecta Distribution Patterns at Meteor Crater, Arizona: On the Applicability of Lithologic End-Member Deconvolution for Spaceborne Thermal Infrared Data of Earth and Mars. *Journal of Geophysical Research* 107: 3.1–3.14. https://doi.org/10.1029/2001JE001827.

Reimold, W. U., and Koeberl, C. 2014. Impact Structures in Africa: A Review. *Journal of African Earth Sciences* 93: 57–175. https://doi.org/10.1016/j.jafrearsci.2014.01.008.

Ringwood, A. E. 1970. Origin of the Moon: The Precipitation Hypothesis. *Earth and Planetary Science Letters* 8: 131–40.

Serefiddin, F., Herzog, G. F., and Koeberl, C. 2007. Beryllium-10 Concentrations of Tektites from the Ivory Coast and from Central Europe: Evidence for Near-Surface Residence of Precursor Materials. *Geochimica et Cosmochimica Acta* 71: 1574–82. https://doi.org/10.1016/j.gca.2006.12.007.

Sturm, S., Wulf, G., Jung, D., and Kenkmann, T. 2013. The Ries Impact, a Double-Layer Rampart Crater on Earth. *Geology* 41: 531–4. https://doi.org/10.1130/G33934.1.

Tian, Z., Chen, H., Fegley, B., Lodders, K., Barrat, J.-A., Day, J. M. D., and Wang, K. 2019. Potassium Isotopic Compositions of Howardite-Eucrite-Diogenite Meteorites. *Geochimica et Cosmochimica Acta* 266: 611–32. https://doi.org/10.1016/j.gca.2019.08.012.

Tyburczy, J. A., Frisch, B., and Ahrens, T. J. 1986. Shock-Induced Volatile Loss from a Carbonaceous Chondrite: Implications for Planetary Accretion. *Earth and Planetary Science Letters* 80: 201–7. https://doi.org/10.1016/0012-821X(86)90104-4.

Tyburczy, J. A., Krishnamurthy, R. V., Epstein, S., and Ahrens, T. J. 1990. Impact-Induced Devolatilization and Hydrogen Isotopic Fractionation of Serpentine: Implications for Planetary Accretion. *Earth and Planetary Science Letters* 98: 245–61.

Vasconcelos, M. A. R., Leite, E. P., and Crósta, A. P. 2012. Contributions of Gamma-Ray Spectrometry to Terrestrial Impact Crater Studies: The Example of Serra da Cangalha, Northeastern Brazil: Gamma-Ray Spectrometry of Impact Craters. *Geophysical Research Letters* 39: L04306. https://doi.org/10.1029/2011GL050525.

Wagner, R., Reimold, W. U., and Brandt, D. 2002. Bosumtwi Impact Crater, Ghana: A Remote Sensing Investigation. In *Meteoritic Impacts in Precambrian Shields*, edited by J. Plado and L. J. Pesonen, 189–210. Heidelberg: Springer.

Wilford, J., Bierwirth, P. N., and Craig, M. A. 1997. Application of Airborne Gamma-Ray Spectrometry in Soil/Regolith Mapping and Applied Geomophology. *Journal of Australian Geology & Geophysics* 17: 201–16.

Woodfield, P. D. 1966. The Geology of the 1⁄4 Field Sheet 91, Fumso N. W. *Ghana Geological Survey Bulletin* 30: 1–66.

Wright, J. B., Hastings, D. A., Jones, W. B., and Williams, H. R. 1985. *Geology and Mineral Resources of West Africa*, 190. Amsterdam, the Netherlands: Springer. https://doi.org/10.1007/978-94-015-3932-6.

Wulf, G., Hergarten, S., and Kenkmann, T. 2019. Combined Remote Sensing Analyses and Landform Evolution Modeling Reveal the Terrestrial Bosumtwi Impact Structure as a Mars-Like Rampart Crater. *Earth and Planetary Science Letters* 506: 209–20.

SUPPORTING INFORMATION

Additional supporting information may be found in the online version of this article.

Fig. S1. Potassium, Th, and U concentrations as a function of depth (data from the geo-chemical database) for felsic intrusives and Ivory Coast tektites.

Fig. S2. Potassium, Th, and U concentrations as a function of depth (data from the geo-chemical database) for lithic impact breccias and Ivory Coast tektites.

Fig. S3. Potassium, Th, and U concentrations as a function of depth (data from the geo-chemical database) for metasedimentary rocks and Ivory Coast tektites.

Fig. S4. Potassium, Th, and U concentrations as a function of depth (data from the geo-chemical database) for regolith and Ivory Coast tektites.

Fig. S5. Potassium, Th, and U concentrations as a function of depth (data from the geo-chemical database) for suevites and Ivory Coast tektites.

Table S1. Bosumtwi geochemical database (data from Jones [1985], Koeberl et al. [1998], Boamah and Koeberl [2002], Dai et al. [2005], Coney et al. [2007], Karikari et al. [2007], McDonald et al. [2007], Ferrière et al. [2010], Losiak et al., 2013).

Table S2. Ground-based measurements (coordinates, lithologies, K, Th, and U from ground-based measurements) and K, Th, and U values (from airborne radiometric at the same location)—includes mean values of each outcrop.

APPENDIX

MODELING EQUATIONS

The concentration of cosmogenic nuclides in the substratum (material below the ejecta deposit, $z > h(t)$) is composed of the decay of the initial concentration profile, $C_i(z)$ (inheritance), and of production of new cosmogenic nuclides between the impact event and present time (second term):

$$C(z, z > h(t)) = C_i(z)e^{-\lambda t} + \frac{P_0}{(\lambda + \nu\epsilon)}\left(1 - e^{-(\lambda+\mu\epsilon)t}\right)e^{-\nu z} \quad \text{(A1)}$$

where P_0 is the surface production rate, λ the decay rate, and ν is the attenuation factor. It is assumed that the substratum, which has been exposed for several millions of years before the impact event, and subjected to a regional erosion state ϵ_r, had reached steady state at the time of impact. The concentration of cosmogenic nuclides in the substratum at the time of impact is given by (steady-state equation):

$$C_i(z) = \frac{P_0}{(\lambda + \nu\epsilon_r)}e^{-(z-h_0+\epsilon t)} \quad \text{(A2)}$$

Combining Equations A1 and A2 leads to the final expression for the concentration of cosmogenic nuclides in the substratum:

$$C(z, z > h(t)) = \frac{P_0}{(\lambda + \nu\epsilon_r)}e^{-(z-h_0+\epsilon t)}e^{-\lambda t} + \frac{P_0}{(\lambda + \nu\epsilon)}\left(1 - e^{-(\lambda+\nu\epsilon)t}\right)e^{-\nu z} \quad \text{(A3)}$$

The concentration of cosmogenic nuclides in the ejecta layer ($z < h$) is given by the decay of existing nuclides in the ejecta layer (inheritance, first term of the equation), and production of cosmogenic nuclides between the impact event and present time:

$$C_r(z,\ z<h(t)) = C_{0e}(z)e^{-\lambda t} + \frac{P_0}{(\lambda+\nu\epsilon)}\left(1-e^{-(\lambda+\nu\epsilon)t}\right)e^{-\nu z} \quad \text{(A4)}$$

where C_{0e} is the initial concentration of the cosmogenic nuclides in the ejecta deposit. The ejecta layer is assumed to initially have a constant concentration of cosmogenic nuclides with depth, resulting from a mixing of material between the preimpact surface ($z = h_0$) and a given thickness of mixing z_m—at $z = h_0 + z_m$. Furthermore, it is assumed that the substratum, which has been exposed for several millions of years, and subjected to a regional erosion state, had reached steady state. The depth-averaged profile of the concentration of cosmogenic nuclides within the substratum just before the impact event returns the average concentration in the ejecta layer of a given cosmogenic nuclide.

$$C_{0e} = \frac{1}{z_m}\int_{h_0}^{h_0+z_m}\frac{P_0}{(\lambda+\nu\epsilon_r)}e^{-(\nu z-h_0)}dz \quad \text{(A5)}$$

$$C_{0e} = \frac{P_0}{z_m\nu(\lambda+\nu\in_r)}(1-e^{-\nu z_m}) \quad \text{(A6)}$$

Combining Equations A4 and A6 leads to the final expression for cosmogenic nuclides in the ejecta layer:

$$C_r(z,\ z<h(t)) = \frac{P_0}{z_m\nu(\lambda+\nu\epsilon_r)}(1-e^{-\nu z_m})e^{-\lambda t} + \frac{P_0}{(\lambda+\nu\epsilon)}\left(1-e^{-(\lambda+\nu\epsilon)t}\right)e^{-\nu z} \quad \text{(A7)}$$

The final equations used in the numerical code account for the respective production of cosmogenic nuclides by neutrons (denoted by subscript *n*), slow (denoted by subscript *s*) and fast muons (denoted by subscript *f*), and are given below. The list of parameters related to ^{10}Be are provided in Table 3.

Within the ejecta layer:

$$\begin{aligned} C_r(z,\ z<h(t)) \ =\ & \frac{P_{0n}}{z_m\nu_n(\lambda+\nu_n\epsilon_r)}(1-e^{-\nu_n\epsilon_r})e^{-\lambda t} + \frac{P_{0n}}{(\lambda+\nu_n\epsilon)}\left(1-e^{-(\lambda+\nu_n\epsilon)t}\right)e^{-\nu_n z} \\ & + \frac{P_{0s}}{z_m\nu_s(\lambda+\nu_s\epsilon_r)}(1-e^{-\nu_s z_m})e^{-\lambda t} + \frac{P_{0s}}{(\lambda+\nu_s\epsilon)}\left(1-e^{-(\lambda+\nu_s\epsilon)t}\right)e^{-\nu_s z} \\ & + \frac{P_{0f}}{z_m\nu_f(\lambda+\nu_f\epsilon_r)}(1-e^{-\mu_f z_m})e^{-\lambda t} + \frac{P_{0f}}{(\lambda+\nu_f\epsilon)}\left(1-e^{-(\lambda+\nu_f\epsilon)t}\right)e^{-\nu_f z} \end{aligned} \quad \text{(A8)}$$

Below the ejecta layer:

$$\begin{aligned} C_r(z,\ z>h(t)) \ =\ & \frac{P_{0n}}{(\lambda+\nu_n\epsilon_r)}e^{-(z-h_0+\epsilon t)}e^{-\lambda t} + \frac{P_{0n}}{(\lambda+\nu\epsilon)}\left(1-e^{-(\lambda+\nu_n\epsilon)t}\right)e^{-\nu_n z} \\ & + \frac{P_{0s}}{(\lambda+\nu_s\epsilon_r)}e^{-(z-h_0+\epsilon t)}e^{-\lambda t} + \frac{P_{0s}}{(\lambda+\nu\epsilon)}\left(1-e^{-(\lambda+\nu_s\epsilon)t}\right)e^{-\nu_s z} \\ & + \frac{P_{0f}}{(\lambda+\nu_f\epsilon_r)}e^{-(z-h_0+\epsilon t)}e^{-\lambda t} + \frac{P_{0f}}{(\lambda+\nu\epsilon)}\left(1-e^{-(\lambda+\nu_f\epsilon)t}\right)e^{-\nu_f z} \end{aligned} \quad \text{(A9)}$$

Results of AMS measurements of ^{10}Be contents in the Bosumtwi impact structure from Serefiddin et al. (2007).

Depth (m)	Sample	Comment on location	Lithologies	^{10}Be (kat g^{-1})
0	LB29A	Moat	Soil	154000 ± 8000
0.50	LB29B	Moat	Soil	395000 ± 23000
0.80–0.90	LB29C	Moat	Soil	386000 ± 25000
0.80–0.90	LB29C	Moat	Soil	437000 ± 23000
0.20	LB52A	Surrounding terrains	Soil	149000 ± 60000
0.50	LB52B	Surrounding terrains	Soil	133000 ± 12000